This is a preprint, the final version is subject to change, of the American Mineralogist (MSA)
Cite as Authors (Year) Title. American Mineralogist, in press.
(DOI will not work until issue is live.) DOI: http://dx.doi.org/10.2138/am-2017-5700

Revision 1.

Uranium bearing opals: Products of U-mobilization, diffusion and transformation processes

Michael Schindler[1*], Mostafa Fayek[2], Britanney Courchesne[1], Kurt Kyser[3] and Frank C. Hawthorne[2]

1. Department of Earth Sciences, Laurentian University, Sudbury, ON, Canada, P3E 2C6
2. Department of Geological Sciences, University of Manitoba, Winnipeg, Manitoba, Canada, R3T2N2
3. Department of Geological Sciences and Geological Engineering, Queen's University, Kingston, ON, K7L 3N6, Canada

*corresponding author

ABSTRACT

Understanding the retention mechanism of U by amorphous silica (i.e. opal) in the environment is of great importance to nuclear-waste disposal because opals can retain U for millions of years. Uraniferous opals from Spor Mountain and the Thomas Range, Utah, USA, are examined in terms of their mineralogical, chemical and isotopic compositions. Uranium-rich zones composed of most likely vorlanite, $CaUO_4$, occur in fibrous opal-CT (termed lussatite) along the interface of the phase with microcrystalline quartz. Red- to black coloured precipitates of vorlanite also occur in the interstices between fibers and grains in lussatite and massy opals, respectively. The high abundance of vorlanite in certain growth zones can be explained by the diffusion of Ca and U along boundaries of layers, grains and fibers and by the release of Ca and U through the transformation of opal-A into opal-CT and from opal-CT into microcrystalline quartz. Similar O-isotope compositions of opal-CT and associated microcrystalline quartz indicate that crystallization processes and deposition of subsequent layers of opal occurred from fluids of similar origin and T. Differences in the isotope and chemical composition between uraniferous opals/microcrystalline quartz, the SiO_2 polymorph moganite, and pyrolusite indicate the past-occurrence of various alteration processes involving fluids of different composition and T. The results of this study indicate that assemblages of opal and microcrystalline quartz can retain U for millions of years as long as confined pore spaces between different generations of opal and quartz or between growth features of opal provide space for the nucleation and adsorption of U-bearing phases and species.

INTRODUCTION

Amorphous silica plays an important role in the retention of radionuclides and metals in aquifer, tailings and soils (e.g. Allard et al 1999; Schindler et al. 2009a; Schindler and Hochella 2015) and can play an important role in the retention of radionuclides in the surroundings of a potential nuclear waste repository (Lichtner and Eigenberg, 1994; Smellie and Karlsson 1999; Techer et al. 2006; Shao et al. 2013). For example, opal has been identified as one of the predominant secondary phases that forms during the alteration of volcanic tuff, a formerly proposed host rock for the repository of high-level nuclear waste at Yucca Mountain, Nevada, USA (Ewing and von Hippel, 2009, Long and Ewing, 2004, MacFarlane and Ewing, 2006). Field studies at the latter location and experimental studies on volcanic tuff have shown that amorphous silica (opal) and calcite are the dominant secondary minerals that form within fractures during evaporation of meteoric water (e.g. Szabo and Kyser, 1990, Paces et al., 2001, Whelan et al., 2002) and through circulation of water in tuff under low-T conditions (< 100ºC), respectively (Dobson et al., 2003). Amorphous silica could also occur at the interface between altered cementitious material and siliceous host rocks of a multi-barrier repository system at a potential nuclear-waste disposal site. Alteration of cementitious material in a repository would result in hyper-alkaline solutions with pH values above 10.5 which could persist over an extended time frame within the repository (10^5-10^6 years; Braney et al., 1993; Schwyn et al., 2012; Smith et al. 2015). Propagation of the hyper-alkaline solutions into the siliceous host rocks would result in the dissolution of silicate minerals, the neutralization of the solutions toward lower pH-values (pH < 9), and precipitation of Ca-silica-bearing phases, including (amorphous) silica along their flow path (Lichtner and Eigenberg, 1994; Smellie and Karlsson 1999; Techer et al. 2006; Shao et al. 2013).

Geochronological studies of U-bearing opals at Yucca Mountain and Spor Mountain, Utah, USA, show that amorphous silica can retain U over millions of years (Zielinski et al. 1977; Ludwig et al. 1980; Paces et al. 2001, 2004) and indicate the significance of amorphous silica

precipitates on long-term retention of U. However, despite many field and experimental studies on the speciation, adsorption and incorporation of U into opal, agate, chalcedony and amorphous silica (Dugger et al. 1964; Zielinski 1980; Ludwig et al. 1980; Michard et al.; 1996; Moll et al. 1998; Reich et al. 1998; Allard et al. 1999; Sylwester et al. 2000; Calas et al. 2008; Soderholm et al. 2008; Schindler et al. 2010; Othmane et al. 2013; Massey et al. 2014; Götze et al. 2015; Schindler et al. 2015), the underlying mechanisms for the incorporation and retention of U by amorphous silica is not yet fully understood.

Previous studies on the adsorption and incorporation of U into amorphous silica

Uranyl-ions have a higher affinity to sorb on silanol groups than many other divalent cations (Dugger et al. 1964, Tran et al. 1999). Maximum adsorption of uranyl-bearing aqueous species on amorphous silica occurs in the pH range 5 to 7 (Michard et al. 1996; Baik and Hahn 2001). The amount of adsorbed uranyl species commonly increases with the number of silica colloids and decreases with the total concentration of U in solution (Baik and Hahn 2001). Adsorption of uranyl ions on amorphous silica in NaCl solution increases with T in the range 5 to 25ºC but decreases between 25 and 65 ºC, whereas their adsorption constantly increases with T in a Na_2CaO_3 solution (Ames et al. 1983). Zielinski (1980) showed that the co-precipitation of amorphous silica with uranyl ions can result in the enrichment of U in the precipitate by factors of 400 to 1000 relative to the concentrations of U in solution.

Adsorbed uranyl ions on the surface of amorphous silica commonly share two O atoms with silica tetrahedra, resulting in an edge-sharing (bidentate) adsorption complex (Massey et al. 2014). Here, the bidentate adsorption complexes $=SiO_2UO_2$ and $=SiO_2UO_2OH$ species seem to predominate under weak acidic solutions whereas the ternary surface complex ($=SiO_2UO_2OHCO_3$) occurs predominantly in the pH range 8.0-8.8 (Gabriel et al. 2001). The crystal-chemical environment of U in amorphous silica varies with the U concentration and the pH in solution as well as with the presence of Fe and Al-(hydr)oxide impurities within the

amorphous silica precipitate. For example, Allard et al. (1999) and Soderholm et al. (2008) identified polymerized uranyl-species in silica gels with elevated concentrations of U (up to 40 wt%) whereas Schindler et al. (2015) showed the common association of uranyl- and arsenate species in amorphous Fe-Al-silica precipitates.

Studies on the speciation of U in U-bearing opals from the Opal Butte Mine in Oregon, USA (U concentrations in the lower $mgkg^{-1}$ range) also showed the presence of bidentate U-silica adsorption complexes (Massey et al. 2014). Conversely higher concentrations of U in opaline rock coatings (in the weight percent range) occur in close association with Ca (Schindler et al. 2010) as a result of the occurrence of nano-crystals of vorlanite, $CaUO_4$,within silica layers enriched in U (Othmane et al. 2013).

Geological and mineralogical background on the occurrence of opal at Spor Mountain

The Spor Mountain district is situated along the western ring-fracture system of the Thomas caldera in Utah, USA, which is part of a group of at least three Oligocene volcanic subsidence structures that together form an east- to west-trending belt of igneous rocks and related mineral deposits. The Thomas Range consists of three groups of volcanic rocks that overlie a Paleozoic sedimentary sequence near Spor Mountain (Lindsey, 1977; Lindsey, 1979; Lindsey et al., 1975; Shawe, 1972). The youngest of the group are the alkali-rhyolite tuffs and flows of the Spor Mountain Formation, which erupted approximately 21 Ma ago, and the Topaz Mountain Rhyolite, which erupted 7.6 Ma ago (Lindsey, 1979). The Spor Mountain Formation consists of two informal members: the lower beryllium tuff member and an upper rhyolite lava-flow member. The tuffaceous breccias and stratified tuffs at Spor Mountain contain Be ore formed as a result of explosive F- and lithophile-rich volcanism that brought ash, carbonate fragments and other lithics to the surface through vent structures in the underlying Paleozoic dolomite rocks (Foley et al. 2012). Hydrothermal fluids are thought to have leached Be from volcanic glass in the tuff and precipitated bertrandite, $Be_4(Si_2O_7)(OH)_2$, where the hydrothermal fluid reacted with carbonate

126 in lithic-rich sections of the tuff. Hydrothermal alteration of the tuff and volcanic glass resulted in
127 the leaching of other elements such as U (typically >10 $mgkg^{-1}$ U). Subsequent interaction of
128 these fluids with dolomite clasts produced layered nodules composed of calcite, Mn-oxides,
129 uraniferous opal and fluorite (Foley et al. 2012).

130 Uraniferous opals occur in 1-2 cm wide fracture fillings in tuffs of the Thomas Range but
131 occur most commonly in the crystal tuff member of the Joy Tuff at the Autunite No. 8 prospect
132 on the east side of Topaz Mountain and in the beryllium tuff member of the Spor Mountain
133 Formation (Ludwig et al. 1980). Calcite, quartz, fluorite, weeksite and perhaps other secondary
134 U minerals are commonly associated with the opal (Zielinski et al. 1977). The opals often show
135 strong zoning of U, which suggests large fluctuations in the supply, rate, or conditions of U
136 precipitation. However, the origin and T of the fluids that resulted in the formation of the
137 uraniferous opals remain uncertain. Foley et al. (2012) argued that if silica, calcite and fluorite
138 were the major phases in equilibrium with the fluids, a likely mechanism for controlling the rate
139 of precipitation of the opals was change in temperature or pressure in fluids of hydrothermal
140 origin. On the other hand, O-isotope compositions of opals at the Autunite No. 8 locality suggest
141 a meteoric-groundwater source with T of 36 °C or less (Henry, 1979). Geochronological studies
142 on the uraniferous opals from Topaz and Spor Mountain showed that groundwater or
143 hydrothermal fluids started to deposit successive opaline layers 21 m.y. ago, during or soon
144 after eruption of the host Spor Mountain Formation and beryllium-fluorite mineralization, and this
145 deposition has continued episodically until 3 m.y. ago (Ludwig et al. 1980).

146 The goals of this study are (1) to characterize the mineralogical, chemical and isotopic
147 composition of uraniferous opals from Spor Mountain and the Thomas Range, Utah, USA., (2)
148 to determine the origin of the fluids that resulted in their formation and (3) to better understand
149 how the distribution of U in opals is affected by transformation processes from opal A via opal
150 CT to microcrystalline quartz.
151

MATERIALS AND METHODS

The opal samples were provided by R. Zielinski and D. Lindsey from the U.S. Geological Survey and were previously characterized by Ludwig et al. (1980) in terms of their U concentration and U-Pb age (Table 1). One altered rhyolite and three uraniferous opal samples are examined in this study using a combination of Electron Microprobe analysis (EMPA), Laser Ablation ICP-MS, Secondary-Ion Mass spectroscopy (SIMS), X-ray Photoelectron Spectroscopy, Scanning Electron Microscopy (SEM), X-ray powder diffraction and Raman Spectroscopy. Table 1 lists the sample location, paragenesis, appearance, U-Pb age and the analytical methods used to characterize each sample.

Scanning Electron Microscopy (SEM), Electron MicroProbe Analysis (EMPA) and X-Ray Diffraction (XRD)

Scanning Electron Microscopy (SEM) was done using a JEOL 6400 SEM operated at 20 kV and with a beam current of ~ 1 nA. The microscope is equipped with both backscattered (BSE) and secondary electron (SE) detectors and an Energy Dispersive X-ray Spectrometer (EDS) and is located in the Central Analytical Facility (CAF) at Laurentian University.

The samples *M3N and DL-U18B* were characterized with a Cameca SX-100 in the Ontario GeoScience Laboratories (Table 1). A wavelength-dispersive spectrometer (WDS) was used to collect data for Na, Mg, Al, Si, K, Ca, Mn, Fe and U at 20kV and 10nA using a focused beam. A PAP correction (Pouchou and Pichoir, 1985) was applied to all data and a decomposition study was done to monitor count-rate changes over time.

Powder X-ray diffraction was done with a Philips PW 1729 X-ray diffractometer using Co *K*α radiation (1.79 Å) at a voltage and current of 40Kv and 30mA, respectively. Spectra from smear-mounted powdered samples were collected over a scan range of 10-70° 2θ with a step size of 0.02 ° 2θ and a dwell time of 2 s.

178 **Conventional stable isotope analyses of the UO_2 standards**

179 The oxygen isotopic composition of pyrolusite, MnO_2 was isotopically characterized by
180 conventional methods at Queen's University, Canada to calibrate it for potential use as an SIMS
181 standard. Oxygen was liberated from multiple fractions of finely powdered (<350 μm) material
182 derived from a single crystal by using the BrF_5 technique of Clayton and Mayeda (1963) and
183 analyzed via dual inlet on a Thermo-Finnigan Delta Plus XP isotope ratio mass spectrometer
184 (IRMS). Oxygen isotopic compositions are reported in units of ‰ relative to Vienna Standard
185 Mean Ocean Water (V-SMOW). Replicate analyses for $\delta^{18}O$ are reproducible to ±0.1‰, and the
186 $\delta^{18}O$ value of NIST-28 quartz is 9.6‰. The oxygen yield for the MnO_2 crystal was 10.7+/-0.2
187 micro moles of O/mg and multiple measurements (3) gave a $\delta^{18}O$ value of -6.8±0.3 ‰.
188

189 **Secondary Ion Mass Spectrometer (SIMS)**

190 Prior to SIMS analysis, the mounts were re-polished and cleaned to remove the carbon
191 coatings and subsequently coated with Au. The mounts were placed in stainless-steel sample
192 holders, and the entire assembly was then placed in the SIMS sample lock and held at high
193 vacuum for a minimum of 8 h prior to the start of the analysis. The oxygen isotopic composition
194 and relative fluorine concentrations of uraniferous opals, the in-house pyrolusite standard, and
195 crystals and finely disseminated pyrolusite (MnO_2) was measured with a CAMECA ims 7f.
196 Secondary-Ion Mass Spectrometer (SIMS) at the University of Manitoba using a Cs^+ primary
197 beam with extreme energy filtering of 200 eV. The ~2 nA primary-ion beam was focused to a 10
198 x 20 μm spot using a 100 μm aperture in the primary column. The Brazil quartz standard has a
199 $\delta^{18}O_{V\text{-}SMOW}$ value of 15.1±0.3‰. The spot-to-spot reproducibility on the quartz standard was
200 ±0.6‰ (1σ). The overall precision and accuracy for each isotope analysis include errors arising
201 from counting statistics of each individual analysis, calibration to a known standard, and
202 uncertainty in deadtime corrections arising from variable count rates. In general, the overall

precision is ±1‰ (2σ), including the spot-to-spot reproducibility of the in-house pyrolusite standard. Values are reported in units of ‰ relative to Vienna-Standard Mean Ocean Water (V-SMOW) (Table 2).

Uranium and silica concentrations were also obtained with the CAMECA 7f. A ~7 nA primary ion beam of O^-, accelerated at 12.5 kV, was focused to a 30 x 30 μm spot using a 100 μm aperture in the primary column. The sample accelerating voltage was +7.95 kV, with electrostatic analyzer in the secondary column set to accept +8.00 kV. The entrance and exit slits were narrowed to obtain flat-top peaks at a mass resolving power of about 1300. Ions were detected with a Balzers SEV 1217 electron multiplier coupled with an ion-counting system with an overall deadtime of 31 ns. The following species were detected sequentially by switching the magnetic field: $^{30}Si^+$and $^{238}U^+$. A typical analysis lasted ~5 minutes, comprising 15 cycles of analysis. NIST 610, 612 and 614 glass standards were used to construct calibration curves and correct for instrumental mass fractionation.

X-ray Photoelectron Spectroscopy

The near-surface chemical composition of the sample *M3N* was characterized with a Kratos Axis Ultra X-ray Photoelectron Spectrometer (XPS) at the University of Manitoba which is equipped with a magnetic-confinement charge-compensation system. The advantages of this system for insulators (*e.g.* uranyl minerals) have been described in detail by Schindler et al. (2009b, c). Spectra of the U 4f electrons were collected at high resolution using monochromatic Al*K*α radiation (1486.6 eV) and the charge-compensation system. Spectra were recorded using 20 sweeps, scan rates per sweep of 200 ms with analyzer pass-energies of 160 eV (U 4f), and large spot sizes and with an aperture size of 110 μm. Resolution for the different pass energies, spot sizes and aperture are listed in detail in Schindler et al. (2009b, c). Shirley background corrections (Shirley 1972) and Gaussian-Lorentzian peak shapes of 60 ± 10% were used to fit

the U 4f spectra. The electrostatic sample-charging (which was not completely compensated by the charge neutralizer) was corrected by setting the binding energy of the C 1s electrons of adventitious C-H species on the sample surface equal to 285 eV (Wagner et al., 1979, Handbook of X-ray photoelectron spectroscopy). The presence and relative proportions of $U^{6+}$and U^{4+} were determined by peak fitting of the U $4f_{7/2}$ spectra using the software Vision 2.2.6. The FWHM values of the bands in the U 4f spectrum vary in the range 1.70-2.00 eV, but were constrained to be equal in each individual spectrum. More details on fitting of the U $4f_{7/2}$ spectra and standard deviations of the binding energies and relative proportions of the U bands are given by Schindler et al. (2009b).

Laser Ablation Inductively Coupled Plasma Spectroscopy

The major and trace-element composition of opal DL-N22 was measured by laser ablation inductively-coupled plasma mass spectrometry (LA-ICP-MS) using a New Wave Nd-YAG 213 nm laser coupled to a quadrupole Thermo X II mass spectrometer. Ablation was done in a He atmosphere and Ar was mixed to the carrier gas before it entered the ICP-MS. Line scans were recorded with a spot size of 10 µm, respectively, using a repetition rate of 10 Hz and an energy density of 11 Jcm^{-2}. The synthetic glass standard NIST610, which contains a nominal trace-element abundance of ~500 $mgkg^{-1}$ was used as the external standard. The standard was ablated under the same conditions at the beginning of each analytical run, intermittently during acquisition, and at the end of each sample. Detection limits for elements depend on the experimental setting of the laser scan and are listed for a similar experimental setting in Durocher and Schindler (2011). Line scans were designed to traverse the different zones of the opal. Integration areas were selected based on chemical differences between the coatings and matrix composition as obtained by SEM-EDS analyses. The breadth of each integration area was determined by monitoring the inflection points of the rise and fall of the Ca and Si peaks. Laser Ablation ICP-MS data are usually quantified by calibrating the counts per second (CPS)

with respect to an internal standard as well as an external standard (e.g. NIST glasses). However, as the samples analyzed in this study are heterogeneous and partly hydrated, no single element could be used as a suitable standard, so only external standards were used. Molar ratios of the elements were calculated from the total counts obtained and the known concentrations in the NIST glass. These were then used to calculate element concentrations by normalizing the sum of the moles to 100%, the underlying assumption being that the samples dominantly contains Si and Ca (as was observed in SEM-EDS analyses). The mole-proportion of H_2O and F^- was estimated on the basis of the number of F^- and H_2O groups per Ca and Si in fluorite and opal-CT. This procedure resulted in a semi-quantitative data set based on the uncertainty of the amount of fluorite and (H_2O) present in the opal.

Raman spectroscopy

Raman spectra recorded at Laurentian University were obtained over the range of 100 to 4000 cm^{-1} and collected in backscattered mode with a HORIBA JobinYvon XPLORA spectrometer interfaced with an Olympus BX 41 microscope, 100x magnification (estimated spot size of 2 µm), a 1200 cm^{-1} grating and an excitation radiation of λ = 532 nm. Calibration was done using the 521 cm^{-1} line of a silicon wafer.

RESULTS

Altered tuff from Spor Mountain (sample RD)

Altered tuff at Spor Mountain and the Thomas range is the host rock of the uraniferous opals and is predominantly composed of K-feldspar, montmorrilonite, fluorite, opal-CT and the Mn-oxides crytomelane and pyrolusite (Fig. 1a, Table 1). The latter minerals occur as strongly altered crystals and as fine precipitates in a fluorite matrix (Fig. 1b), whereas opal-CT is either intergrown with montmorillonite or contains small inclusions of the clay mineral. Hence, the O-isotope compositions of opal-CT and montmorillonite could not be unequivocally determined.

The O-isotope compositions of altered crystals and finely disseminated pyrolusite were measured and found to be very similar with $\delta^{18}O$ values of -8.6±0.8 and -8.9±1.6‰, respectively. The $\delta^{18}O$ value for the finely disseminated pyrolusite will be used to further explore the T of formation for the uraniferous opal and associated silica modifications (see below).

Sample *DL-U18B* from the Thomas Range

The sample *DL-U18B* is composed of white to violet-coloured U-bearing opals (mainly opal-CT) in close association with microcrystalline quartz, moganite and K-feldspar (Fig. 1c). Its average U concentration is 0.1 wt% (on the basis of 24 spot analyses) whereas violet-colored areas can contain up to 0.3 wt% U (Table 2). Variations in chemical composition of the opal-CT are shown in chemical distribution maps for Ca and U and SEM images in backscatter mode, which indicate the common occurrence of U and Ca (Figs. 1d-e, 2a-b), especially along boundaries between zones enriched and depleted in both elements. The common occurrence of U and Ca can be also recognized in a plot with the concentrations of U versus Ca (Fig. 1f). The background concentrations for Ca are ~7 mmol (*i.e*. the concentrations for Ca when the concentrations of U are below the detection limit, Fig. 1f) and may be the result of traces of fluorite or adsorbed Ca species in the opaline matrix. Uranium concentrations, $\delta^{18}O$ values (11 measurements) and Raman spectra (8 spectra) were recorded along a traverse across two zone boundaries enriched in U and Ca (labelled *A1-A6* and *B1-B2* in Fig. 2a-d). In the Raman spectra (Fig. 2d), the main peaks for opal-CT occur between 200 and 420 cm^{-1} (labelled *OP*) and those for quartz (Q) and moganite (*M*) at 465 and 501 cm-1, respectively (*e.g*. Kingma and Hemly 1994, Ilieva et al. 2007 and references therein). Closer inspection of the latter spectra (Fig. 2d) and the chemical distribution map for U (Fig. 2b) indicate that higher concentrations of U occur in areas predominantly composed of opal-CT (areas *A2* and *A4*), whereas areas composed of predominantly quartz and moganite are depleted in U relative to opal-CT (*A1, A5-*

A6, B1-B2). Contrary the values for $\delta^{18}O$ are similar in areas predominantly composed of quartz and opal-CT (*A1-A6,* Table 2) but drop to lower values towards the area composed of mainly moganite (*B1-B2*). The area labelled *B1* may be considered as a transition zone between quartz and moganite as the corresponding Raman spectrum does not display well resolved peaks for either quartz or moganite (Fig. 2d) and its $\delta^{18}O$ values are slightly lower and higher than in the areas predominantly composed of quartz and moganite, respectively (Fig. 2c; Table 2).

The structural components of cristobalite and tridymite in opal-CT can be identified in the Raman spectra (Fig. 3a-c; e.g. Ilieva et al. 2007) and X-ray diffraction pattern (Fig. 3d; for details see Flörke et al., 1991; Graetsch,1994; Lynne and Campbell, 2004). In XRD pattern for opal-CT, intensity bands at 4.1 and 2.5 Å are representative of cristobalite and tridymite stacking sequences (Flörke et al., 1991). The band at 4.1 Å is commonly composed of a peak at 4.1 Å and a shoulder at 4.2-4.3 Å corresponding to the (101) and (-4-04) d-spacings in cristobalite and tridymite, respectively. However, the use of Co Kα rather than Cu Kα radiation (smaller radius of the Ewald sphere) allowed a better resolution of the cristobalite and tridymite structural components in the band at 4.1 Å (Fig. 3d). Raman spectrum for area *A4* and the XRD spectra for the samples *M3N*, *DL-U18B* and *DL-N22* indicate the presence of both structural components in the opal-CT whereby the Raman spectrum suggests a higher proportion of the trydimite component in area *A4* (Fig. 3a) and the XRD bands higher proportions of the cristobalite component in the bulk materials (Fig. 3d).

Opal-CT commonly forms two texturally distinct modifications: fibrous opal-CT, termed lussatite, forms bundles of fibres (upper nm-scale) whereas massy opal-CT comprises of small thin platelets forming lepispheric aggregates between 1 and 10 µm in diameter. High-resolution optical images of an area in proximity to the examined traverse indicate that opal-CT occurs as bands of lussatite which are over- and underlain by bands of microcrystalline quartz (Fig. 4a). An image taken at higher magnification indicates that the interface between lussatite and quartz

is sharp at the micrometer scale (Fig. 4b). Small red-coloured crystals occur along this interface or are embedded in the fibrous matrix of the lussatite in proximity to the interface (Fib. 4b).

Sample *M3N* from Spor Mountain

Opal sample *M3N* consists of a core of purple fluorite and opal-CT (~ 80 $mgkg^{-1}$ U), which is surrounded by a white opal-CT with minor fluorite (~200 ppm U) and an outer shell of a yellowish-brown fluorescent opal-CT (Ludwig et al. 1980). A fragment of the outer shell (Fig. 5a) contains on average 3011 $mgkg^{-1}$ U with areas reaching concentrations up to 6342 $mgkg^{-1}$ U (Table 2). Chemical-distribution maps show a close association of U and Ca in clusters within the silica matrix of the outer shell (Figs. 5b, c). Quantitative analyses of 24 EMPA measurements indicate a linear correlation between the concentrations of both elements (Fig. 5e) with background concentrations for Ca of 5 $mmol^{-1}$. Uranium concentrations, F / O CPS ratios and $\delta^{18}O$ values were measured along a traverse in one of the corners of the sample (Fig. 5). Although the concentrations of U and values for $\delta^{18}O$ vary significantly (U varies between 1600 and 2600 $mgkg^{-1}$ and $\delta^{18}O$ between 11 and 20 ‰), they do not correlate along the traverse (Figs. 5f and g). Raman spectra (not shown) and XRD pattern (Fig. 3d) indicate the presence of only opal-CT and a high-resolution optical image reveals the presence of massy opal (Fig. 4a). Closer inspection of the latter image reveals the presence of black-coloured precipitates in the interstices between the blade-like grains of the opal.

Figure 6 shows U4f $_{7/2}$ spectra of sample *M3N* and of a yellow and green uraniferous opal from Pena Blanca which also contain Ca and U in a 1 : 1 ratio (Schindler *et al*. 2010). The envelopes for the opals from Pena Blanca depict a maximum and shoulder at 393.5 and ~391.5 eV, respectively. Maximum and shoulder were fitted with bands representing U^{6+} and U^{4+}/U^{5+} components in the surface structure of the opals, respectively. Note that the satellite peaks for U^{6+}, U^{5+} and U^{4+} were not resolved in the U 4f spectra for the opals, a common observation for samples containing U concentrations below ~3 wt% (Schindler et al. 2009b). Contrary to the

356 spectra for the opals from Pena Blanca, the envelope of the U4f $_{7/2}$ spectrum for sample *M3N*
357 does not show any shoulder at the lower binding energy-side and its envelope was thus fitted
358 with only one band representing U^{6+}.
359
360 **Sample *DL-N22* from Spor Mountain**
361 Sample *DL-N22* contains white to purple zones in which the proportion of fluorite
362 increases with the intensity of the violet colour. Bertrandite and a finely disseminated Mn-oxide
363 were detected with XRD (> 5 modal %) and SEM in the bluish-black outer rim of the sample
364 (Fig. 7a, 8c), respectively. Inspection of the LA-ICP-MS line-scan pattern for Si, Ca (Fig. 7b) and
365 Mn (not shown) indicates that the sample may be divided into three chemically distinct zones
366 (Figs. 7a, b): Zone A with a white shade contains more Si than Ca (mole %), zone B is violet
367 and contains equal proportions of Si and Ca, and zone C is bluish-black and contains
368 predominantly fluorite. Quantification of the LA-ICP-MS data (see above) indicates that zone *B*
369 contain the highest concentrations in U with 1200 $mgkg^{-1}$ U followed by zones *A* and *C* with U =
370 860 and 790 $mgkg^{-1}$, respectively. Closer inspection of the line scans indicates that the interface
371 between zones *B* and *C* (encircled) is enriched in U relative to the central parts of the latter
372 zones. The similarities in the pattern for the line scans of Ca and U (Fig. 7b) as well as a
373 correlation between the concentrations for Ca [wt%] and U [$mgkg^{-1}$] (Fig. 8a) indicate a close
374 association between U and Ca. Uranium concentrations, F / O CPS ratios and $\delta^{18}O$ values were
375 recorded along a traverse from zone *A* to the interface between zones *B* and *C* (Fig. 7c-e). The
376 oxygen isotopic composition remains relatively constant along the traverse whereas the
377 concentrations of U and the CPS ratios of F / O are higher closer to the interface between zones
378 *B* and *C*. Interestingly, maximum values for the concentrations of U and the CPS ratios of F / O
379 do not coincide, suggesting that higher concentrations of U are not necessarily associated with
380 areas enriched in fluorite, bertrandite and an unidentified Mn-oxide intergrown in zone *C* (Fig.
381 8c). A plot of the concentration of Mn versus U indicates an inverse correlation for Mn-

concentrations above 0.8 wt% (Fig. 8b), suggesting that areas enriched in MnO_x are depleted in U relative to areas enriched in opal. Raman spectra (not shown), XRD pattern (Fig. 3d) and optical image (Fig. 4a) indicate again the occurrence of a massy modification of opal-CT that contains small red-black coloured precipitates in the interstices of the blade-like grains.

Degree of structural ordering in the examined of opal-CT

The full width at half-maximum intensity (FWHM) of the ~4 Å diffraction band can be used as a guide to the degree of lattice order/disorder within each silica phase, with narrower FWHM values indicative of greater degree of ordering (Elzea et al., 1994; Graetsch et al., 1994). Typical FWHM values for opal-A are 1.31 ± 0.02, for opal-CT 0.27 ± 0.06 and 0.05 ± 0.01 for opal-C. Following this guide, the FWHM values listed in Figure 3d indicate that lussatite in sample *DL-U18b* has the lowest degree of disorder followed by the massy opals in the samples *M3N* and *DL-N22*.

DISCUSSION

U speciation and mineralogy in the opals

Ludwig et al. (1980) noted the absence of uraninite in fillings around the Be-ore deposits at the Thomas range and Spor Mountain, and concluded that U occurred exclusively in the hexavalent state during the formation of the uraniferous opal. Their conclusion is in accord with the result of the U $4f_{7/2}$ spectrum for the *M3N* sample which also indicates the exclusive occurrence of U^{6+} in the surface structure of the opal sample (Fig. 5a).

The close association of U and Ca is apparent in all three samples (Figs. 1, 5 and 7). The regression analyses for the data from samples *M3N* and *DL-U18B* indicate that an increase or decrease in the concentrations for U and Ca follow an elemental ratio of 1 : 1. The following observations suggest that the Ca-U^{6+}-bearing phase in the three opal samples is predominantly composed of crystals of vorlanite.

(1) The occurrence of red-black coloured crystals or precipitates in the Ca-U-rich zones of the samples *DL-U18B* and *DL-N22;*

(2) The occurrence of black precipitates and U^{6+} in the interior and surface structure of the opal *M3N,* respectively;

(3) Vorlanite forms black crystals which appear brownish-red in thin sections (Galuskin et al. 2011);

(4) There are no known Ca-uranyl-silicate minerals with a Ca: U ratio of 1 : 1;

(5) Uranium-enriched rims with Ca: U ratios of 1 : 1 also exist in opaline rock coatings on volcanic tuff at Pena Blanca, in which vorlanite nanocrystals occur (see above; Calas et al. 2008; Schindler et al. 2010; Othmane et al. 2013).

Vorlanite, cubic $CaUO_4$, is a rare calcium uranate (Othmane et al. 2013). It has a fluorite-type structure and is thus isostructural with uraninite. The structure contains U^{6+} in [8]-coordination with the O atoms equidistant. Othmane et al. (2013) argued that vorlanite formed in a low-T environment from Ca-U rich solution during opal maturation as the latter opals formed around 30 °C on the surface of the volcanic tuff at Pena Blanca (Calas et al. 2008; Schindler et al. 2010). Experimental studies on the formation of phases in the U(VI)-Ca^{2+}-SiO_2-H_2O system indicate that calcium uranates form at pH values above pH 8 (Ritherdon *et al.* 2003). On the basis of thermodynamic data listed for $CaUO_4$ (Navrotsky et al. 2013) and the dissolution reaction $CaUO_4 + 2H_2O \leftrightarrow Ca^{2+} + (UO_2)^{2+} + 4H^+$ the calculated solubility constant for vorlanite is log K = -152.2, which is much lower than the solubility constants of other Ca-uranyl minerals such as becquerelite (log K = 42.08) and uranophane (log K = 7.9) (Gorman-Lewis et al. 2008). The absence of vorlanite in many vadose zones of U-ore deposits, U mine tailings and U-contaminated sites indicate, however, that its formation is kinetically less favoured than those of e.g. becquerelite and uranophane.

433 **Origin and Nature of the fluids that resulted in the alteration of the rhyolite and the**
434 **formation of the opals**

435 It is commonly believed that amorphous silica and fluorite at Spor Mountain and the
436 Thomas Range precipitated from hydrothermal fluids which became supersaturated with respect
437 to both phases during cooling and/or interaction with earlier-formed phases (Ludwig *et al.* 1980,
438 Lindsey 1982, Foley *et al*. 2012). This argument is based on the fact that decreasing stability of
439 F-bearing aqueous species during cooling of hydrothermal fluids commonly results in
440 supersaturation and precipitation of F-bearing minerals (depending on other factors such as
441 ionic strength and the presence of other complexing agents in solution; Nordstrom and Jenne
442 1977). The occurrence of altered crystals and finely disseminated pyrolusite with similar O-
443 isotope composition (Fig. 1b) suggests that (I) the isotope composition and T of the Ca-F-
444 bearing fluids did not significantly change from the initial deposition of the pyrolusite to the
445 dissolution and reprecipitation of the Mn-oxide mineral and thus during multiple alteration
446 processes of the rhyolite or (II) the isotope composition of a first generation of pyrolusite crystals
447 was overprinted by the isotope composition of subsequent fluids which reprecipitated the
448 mineral within a fluorite matrix. In any case, if silica-rich water caused the alteration, dissolution
449 and reprecipitation of the pyrolusite and the formation of opal CT, quartz and moganite at both
450 locations, the T of their formation can be calculated using the measured $\delta^{18}O$ values for the
451 opals, quartz, moganite and pyrolusite, and the amorphous silica-H_2O, oxygen-isotope
452 fractionation factor of Kita et al. (1985) and the pyrolusite-H_2O oxygen-isotope fractionation
453 factor of Zheng (1991).

454 The traverse across two U-enriched boundaries on the surface of opal sample *DL-U18B*
455 indicates a plateau with an average value for $\delta^{18}O$ of 19.8 ‰ (zones *A1-A6),* followed by a drop
456 toward 9.6 ‰ (zones *B1-B2*; Fig. 2c; Table 2). Using the average $\delta^{18}O$-value of -8.9‰ for the
457 finely disseminated pyrolusite, the corresponding temperatures for the formation of the silica
458 phases in the zones *A1-A6* and *B2* are of 0±10ºC and 114±10ºC respectively. The later T

seems reasonable as thermodynamic modeling predict a decreasing solubility of amorphous silica in fluids at Spor Mountain at T below 130°C (Wood 1992).The exceptionally low temperature calculated for the formation of opal-CT and quartz in the zones *A1-A6* suggests, however, that these silica phases did not form from or equilibrate with the fluids that dissolved and re-precipitated the pyrolusite. Furthermore, the abrupt change in the mineralogy, O-isotope composition and concentration of U between the zones predominantly composed of moganite (*B2*) and those of quartz and opal-CT (*A1-A6*) indicate that these two mineral assemblages must have been formed from fluids of different T, isotope composition and U concentration.

Model for the formation of opal-CT, quartz and moganite in sample DL-U18B.

Hardening of freshly-precipitated silica from low-T aqueous solution results commonly in the formation of opal A which transforms into microcrystalline quartz in the sequence opal-A → opal-CT/-C → microcrystalline quartz (Williams et al., 1985; Flörke et al., 1991; Cady et al., 1996; Lynne & Campbell, 2004). This transformation sequence is the most widely known mechanism for the formation of chert rocks, with the initial silica precipitate converting to crystalline quartz (Iijima and Tada, 1981; Knauth, 1994; Hattori et al., 1996). In volcanic environments, however, opal-CT/-C can form directly from high T fluids without the formation of the opal-A precursor. The transformation of opal-A into opal-C/CT and microcrystalline quartz has been recognised as a series of complex dissolution-precipitation events (Stein and Kirkpatrick, 1976; Williams et al., 1985; Williams and Crerar,1985; Hendry and Trewin. 1995). Moganite is a monoclinic SiO_2 polymorph (Miehe and Graetsch, 1992), which is a common component in microcrystalline opaline and quartz modfications such as agate, chalcedony, chert, and flint (Heaney and Post 1992).

The occurrence of a mineralogical transition zone associated with a sudden change in the $\delta^{18}O$ value (zone *B1*) between areas composed predominantly of moganite (zone *B2*) and quartz (zone *A6*) (Fig. 2) suggests that both minerals were formed at different stages. Contrary,

485 similar $\delta^{18}O$ values for opal-CT and quartz in the zones *A1-A6* indicate that the deposition of
486 subsequent bands of opal-CT and their transformation into quartz in the zones *A1, A5-A6*
487 occurred in the presence of fluids of similar O-isotope composition and T. The occurrence of
488 quartz in bands over- and underlying bands of opal-CT may be explain with the deposition of
489 either opal-CT (at high T) or opal-A (at low T) at various stages and the transformation of earlier
490 formed opal-CT into microcrystalline quartz.
491
492 **Models for the formation of the U enriched rims, zones and clusters in the opals**
493 The internal structure of sintered silica reflects the mechanism of coalescence of the silica
494 nanospheres during dehydration of the colloidal silica. In a diffusion-limited aggregation of
495 nanoparticles, the contact regions between the nanospheres became curved, and strings of
496 peanut-shaped units or spherical particles are generated (VanDamme, 2000). Local curvatures,
497 layering and spherical clusters of silica occur in all samples (Figs. 1, 2, 5, 7). The curvatures
498 and layers observed in samples *DL-U18B* and *DL-N22* indicate that layers of opal-CT formed at
499 a later stage adapted to the morphology of the earlier formed layers of opal-CT/microcrystallline
500 quartz.
501 High-resolution optical images suggest that vorlanite formed in the interstices between
502 either individual grains or fibers of massy opal-CT and lussatite, respectively, or along the
503 interfaces between layers of earlier and later formed phases (Fig. 4); i.e. between the interfaces
504 of the zones *A1-A2* and *A4-A5* in *DL-U18B* (Fig. 2) and *B* and *C* in *DL-N22* (Fig. 7). The latter
505 type of occurrences may be explained with three different types of formation mechanisms:
506 I. Diffusion of Ca and uranyl species occurred preferentially along interfaces of opal-CT
507 to quartz (*A1-A2*, *A4-A5* in *DL-U18B*, Fig. 2, 4b) and opal-CT to fluorite (*B*-C in *DL-*
508 *N22*; Fig. 7) and between fibers and bladed grains of lussatite and massy opal,
509 respectively (Fig. 3a and 5b and c) as these interfaces contains larger pore spaces

than the interior of fibers and grains of lussatite and massy opal (e.g. Fischer 1951), respectively;

II. Uranyl-and Ca species entered the system at a later stage along the interfaces *A2-A3*, *A3-A4* (in *DL-U18b*) and *A-B* (in *DL-N22*) and subsequently diffused parallel to the grains and fibers of the massy opal and lussatite towards the interfaces *A1-A2*, *A4-A5* (in *DL-U18B*) and *B-C* (in *DL-N22*). The lower porosity of the microcrystalline quartz (*A1*, *A5-A6* in *DL-U18B*) and fluorite-bertrandite zone layers (*C* in *DL-N22*) acted then as diffusion barrier which resulted in the subsequent nucleation of vorlanite.

III. Uranyl- and Ca aqueous species were released during the transformation of opal-A to opal-CT (all samples) and opal-CT to quartz (*DL-U18B*) and accumulated in the interstices of layers and grains during the transformation process.

Similar average O-isotope compositions of the opals and in particular in the zones *A1* to *A6* in *DL-U18B* (Fig. 2c) and *A* to *C* in *DL-N22* (Fig. 7c; Table 2) suggest that Ca and U-bearing aqueous species were transported by the same fluids as the deposited opals. Hence, mechanism II seems unlikely. Mechanism I most likely resulted in the accumulation of vorlanite along the interfaces *A1-A3*, *A4-A5* (sample DL-U18B, Fig. 2b, 3b) and *B-C* (DL-N22; Fig. 7b). A combination of mechanisms I and III may have resulted in the accumulation of vorlanite along the interfaces of fibers and grains in lussatite and massy opal-CT in the samples *DL-U18B, DL-N22* and *M3N*, respectively (Fig. 3a, 5b and c).

Implications

The work of Ludwig et al. (1980) and Paces et al. (2001, 2004) indicate that secondary opals in volcanic environments can preserve U inclusions over millions of years. The results of our study indicates that retention and mobilization of U within silica precipitates strongly depend on transformation reactions between the phases opal A → opal-C/CT → microcrystalline quartz.

Our study further suggest that U can be retained for millions of years if it becomes trapped between different generations of opaline layers or between grains and fibers of opal modifications at relative stable P-T conditions and low fluid activities. However, transformation of opal to microcrystalline quartz can also result in the release of U when the associated dissolution-reprecipitation reaction occurs during interaction with high T fluids in an open system. The retention mechanism of U by amorphous silica in the environment seems not to resemble mechanisms observed in experimental studies as the majority of U occurs along boundaries between different generations or growth features of amorphous silica. Hence, a quantitative relation between the retention of U by amorphous silica and time can be established only through (a) more studies of naturally occurring uraniferous opals, and (b) experimental studies that involve the formation of different generations of U-bearing amorphous silica.

ACKNOWLEDGMENTS

This work was supported by Discovery Grants to MS, MF, KK and FCH from the Natural Sciences and Engineering Research Council of Canada, Canada Research Chairs to MF and FCH, and CFI grants to FCH. We are indebted to Robert Zielinski and Dave Lindsey for providing the opal samples, to Michael Freund for the use of the XPS spectrometer in his laboratory at the University of Manitoba, and Ryan Sharpe for his help with collecting the SIMS data.

REFERENCES CITED

Allard, T., Ildefonse, P., Beaucaire, C., and Calas, G. (1999) Structural chemistry of uranium associated with Si, Al, Fe gels in a granitic uranium mine. Chemical Geology,158, 81-103.

560 Ames, L.L., McGarrah, J.E., and Walker, B.A. (1983) Sorption of Trace Constituents from
561 aqueous solutions onto secondary minerals. I. Uranium. Clays and Clay Minerals, 31,
562 321-334.
563 Baik, M.H. and Hahn, P.S. (2001) Experimental study on Uranium sorption onto silica colloids:
564 Effects of geochemical parameters. Journal of the Korean Nuclear Society, 33, 261-269.
565 Braney M. C., Haworth A., Jefferies N. L. and Smith A. C. (1993) A study of the effects of an
566 alkaline plume from a cementitious repository on geological materials. Journal of
567 Contaminated. Hydrology, 13, 379–402.
568 Calas G., Agrinier P., Allard T. and Ildefonse P. (2008) Alteration geochemistry of the Nopal I
569 uranium deposit (Sierra Pena Blanca, Mexico), a natural analogue for a radioactive
570 waste repository in volcanic tuffs. Terra Nova, 20, 206-212.
571 Cady, S. L., Wenk, H.-R. and Downing, K. H. (1996) HRTEM of microcrystalline opal in chert
572 and porcelanite from the Monterey Formation, California. American Mineralogist. 81,
573 1380 - 1395.
574 Clayton, R.N. and Mayeda, T.K. (1963)The use of BrF5 in the extraction of oxygen from oxides
575 and silicates for isotopic analysis. Geochimica et Cosmochimica Acta, 27, 43-52.
576 Durocher, J. and Schindler, M. (2011): Iron-hydroxide, Iron-sulfate and hydrous silica coatings in
577 acid-mine tailings facilities: a comparative study of their trace-element composition.
578 Applied Geochemistry, 26, 1337-1352.
579 Dobson P.F., Kneafsey T.L., Sonnenthal E.L., Spycher N. and Apps J.A. (2003) Experimental
580 and numerical simulation of dissolution and precipitation: implications for fracture sealing
581 at Yucca Mountain, Nevada. Journal of Contaminated Hydrology, 62-63, 459-476.
582 Dugger D.L., Stanton J.H., Irby B.N., McConell B.L., Cummings W.W. and Maatman, R.W.
583 (1964) The exchange of twenty metal ions with the weakly acidic silanol group of silica
584 gel. Journal of Physical Chemistry, 68, 757-760.

585 Elizea, J. M., Odom, I. E. AND Miles, W. J. 1994. Distinguishing well ordered opal-CT and opal-C
586 from high temperature cristobalite by x-ray diffraction. Analytica Chimica Acta. 286, 107 -
587 116.
588 Ewing, R.C. and van Hippel, F.N. (2009) Nuclear Waste Management in the United States-
589 Starting Over. Science 325, 151-152.
590 Fisher J. C. (1951) Calculation of Diffusion Penetration Curves for Surface and Grain Boundary
591 Diffusion. Journal of Applied Physics, 22, 74-77.
592 Flörke, O. W., Graetsch, H., Martin, B., Röller, K. and Wirth, R. (1991) Nomenclature of
593 microcrystalline and non-crystalline silica minerals, based on structure and
594 microstructure. *N*eues Jahrbuch für Mineralogische Abhandlungen.163, 1, 19 - 42.
595 Foley, N.K., Hofstra, A.H., Lindsey, D.A., Seal, R.R., II, Jaskula, Brian, and Piatak, N.M. (2012)
596 Occurrence model for volcanogenic beryllium deposits, chap. F *of* Mineral deposit
597 models for resource assessment: U.S. Geological Survey Scientific Investigations
598 Report 2010–5070–F, 43 p.
599 Gabriel, U.,Charlet, L., Schläpfer, C.W., Vial, J.C., Brachmann, A. and Geipel, G. (2001) Uranyl
600 Surface Speciation on Silica Particles Studied by Time-Resolved Laser-Induced
601 Fluorescence Spectroscopy. Journal of Colloid and Interface Science, 239, 358–368.
602 Galuskin, E., Armbruster, T., Galuskina,T.O., Lazic, B., Winiarski, A., Gazeev, V.,
603 Dzierżanowski, P., Zadov, A., Pertsev, N., Wrzalik, R., Gurbanov, A.G., and Janeczek, J.
604 (2011) Vorlanite (CaU^{6+})O_4—A new mineral from the Upper Chegem caldera, Kabardino-
605 Balkaria, Northern Caucasus, Russia. *American Mineralogist, 96, 188–196.*
606 Gorman-Lewis, D., Burns,P.C. and Fein. J.B. (2008) Review of uranyl mineral solubility
607 measurements Journal of Chemical Thermodynamics 40, 335–352.
608 Graetsch, H. (1994) Structural characteristics of opaline and micro-crystalline silica minerals. In:
609 Heaney, P. J., Prewitt, C. T. & Gibbs, G. V. eds. Silica. Physical Behaviour,
610 Geochemistry and Materials Applications, Reviews in Mineralogy, 29, 209 - 232.

611 Graetsch, H., Glies, H. and Topalovi, I. (1994) NMR, XRD and IR study on microcrystalline
612 opals. Physical Chemistry of Minerals. 21, 166 - 175.
613 Götze, J, Gaft, M. and Möckel, R. (2015) Uranium and uranyl luminescence in
614 agate/chalcedony. Mineralogical Magazine, 79, 985–995.
615 Hattori, I., Umeda, M., Nagakagawa, T. and Yamamoto, H. (1996) From chalcedonic chert to
616 quartz chert: diagenesis of chert hosted in a Miocene volcanicsedimentary succession,
617 central Japan. Journal of Sedimentary Research. 66, 1, 163 - 174.
618 Heaney, P.J., and Post, J.E. (1992) The widespread distribution of a novel silica polymorph in
619 microcrystalline quartz varieties. Science, 255, 441-443.
620 Hendry, J. P. and Trewin, N. H. (1995) Authigenic quartz microfabrics in Cretaceous turbidites:
621 evidence for silica transformation processes in sandstones. Journal of Sedimentary
622 Research. A65, 2, 380 - 392.
623 Henry, C.D. (1979) Origin of uraniferous opal, Final Report, Formation of Uranium Ores by
624 Diagenesis of Volcanic Sediments, C.D. Henry and A.W. Walton, eds., U.S. Dep.Energy
625 Rep. GJBX22 (79) Chapters 10, 22.
626 Iijima, A. and Tada, R. (1981) Silica diagenesis of Neogene diatomaceous and volcaniclastic
627 sediments in northern Japan. Sedimentology. 28, 185 - 200.
628 Ilieva, A., Mihailova, B.,Tsintsov Z., and Petrov, O. (2007) Structural state of microcrystalline
629 opals: A Raman spectroscopic study American Mineralogist, 92, 1325.1333.
630 Kingma, K.J. and Hemley, R.J. (1994). Raman spectroscopic study of microcrystalline silica
631 American Mineralogist, 79, 269-273.
632 Kita, I., Taguchi S. and Matsubaya O. (1985) Oxygen isotope fractionation between amorphous
633 silica and water at 34-93ºC. Nature, 314, 83-84.
634 Knauth, P. (1994) Petrogenesis of chert. In: Heaney, P. J., Prewitt, C. T. & Gibbs, G. V.eds.
635 Silica. Physical Behaviour, Geochemistry and Materials Applications. Reviews in
636 Mineralogy, 29. 233 – 258.

637 Lichtner, P.C and Eikenberg, J. (1994) Propagation of a Hyperalkaline Plume into the
638 Geological Barrier Surrounding a Radioactive Waste Repository. National Cooperative
639 for the Disposal of Radioactive Waste Technical Report 93-16, 57pp
640 Lindsey, D.A., Naeser, C.R., and Shawe, D.R. (1975) Age of volcanism and mineralization in
641 the Thomas Range, Keg Mountain, and Desert Mountain, western Utah: U.S. Geological
642 Survey Journal of Research, 3, 75–597.
643 Lindsey, D.A. (1977) Epithermal beryllium deposits in water-laid tuff, western Utah: Economic
644 Geology, 72, 219–232.
645 Lindsey, D.A. (1979) Preliminary report on Tertiary volcanism and uranium mineralization in the
646 Thomas Range and northern Drum Mountains, Juab County, Utah. U.S. Geological
647 Survey Open-File Report 79–1076, 101 pp.
648 Lindsey, D.A. (1982) Tertiary volcanic rocks and uranium in the Thomas Range and northern
649 Drum Mountains, Juab County, Utah: U. S. Geological Survey Professional Paper 1221,
650 71 pp.
651 Long, J.C.S. and Ewing, R.C. (2004) Yucca Mountain: Earth Science Issues at a Geologic
652 Repository for High-Level Nuclear waste. Annual Review Earth and Planetary Science
653 32, 363-401.
654 Ludwig, K.R., Lindsey, D.A., Zielinski, R.A., and Simmons, K.R. (1980) U-Pb ages of
655 uraniferous opals and implications for the history of beryllium, fluorine, and uranium
656 mineralization at Spor Mountain, Utah: Earth and Planetary Science Letters 46, 221–
657 232.
658 Lynne, B. Y. and Campbell, K. A. (2004) Morphologic and mineralogic transitions from opal-A to
659 opal-CT in low-temperature siliceous sinter diagenesis, Taupo volcanic zone, New
660 Zealand. Journal of Sedimentary Research. 74, 561 - 579.

Massey, M.S., Lezama-Pacheco, J.S., Nelson, J.M.,Fendorf, S., and Maher, K. (2014) Uranium incorporation into amorphous silica Environmental Science and Technology, 48, 8636-86344.

Macfarlane A.M. and Ewing R.C. (2006) Uncertainty underground-Yucca Mountain and the Nation's High-Level Nuclear Waste. MIT Press, Cambridge, MA, 431 p.

Michard, P., Guibal, E., Vincent, T., and Le Cloirec, P. (1996**)** Sorption and desorption of uranyl ions by silica gel: pH, particle size and porosity effects. Microporous materials, *5*, 309–324.

Miehe, G., and Graetsch, H. (1992) Crystal structure of moganite: A new structure type for silica. European Journal of Mineralogy, 4, 693-706

Moll, H., Geipel, G., Brendler, V., and Nitsche, B.H. (1998) Interactions of uranium(VI) with silicic acid in aqueous solutions studied by time-resolved laser-induced fluorescence spectroscopy (TRLFS). Journal of Alloys Compounds, 271-273, 765-768.

Navrotsky, A., Schvareva, T. and Guo, X. (2013) Thermodynamics of Uranium Minerals and Related Materials. Uranium – Cradle to Grave, Chapter: 5, Publisher: Mineralogical Association of Canada, Editors: P. C. Burns, G. E. Sigmon, pp.147-164

Nordstrom, D.K. and Jenne, E. (1977) Fluorite solubility equilibria in selected geothermal waters. Geochimica et Cosmochmca Acta, 41, 175-188.

Othmane, G., Allard, T.**,** Menguy, N., Morin, G., Esteve, I., Fayek, M., and Calas, G**.** (2013) Evidence for nanocrystals of vorlanite, a rare uranate mineral, in the Nopal I low-temperature uranium deposit (Sierra Peña Blanca, Mexico). American Mineralogist*,* 98, 518–521.

Paces, J.B., Neymark, L.A., Marshall, B.D., Whelan, J.F. and Peterman, Z.E. (2001) Ages and origins of calcite and opal in the exploratory studies facility tunnel, Yucca Mountain, Nevada. *U.S.* Geological Survey Water-Resource Investment Report 01-4049.

686 Paces, J.B., Newmark, L.A., Wodden, J.L. and Persing, H.M. (2004) Improved spatial resolution
687 for U-series dating of opal at Yucca Mountain, Nevada, USA, using ion-microprobe and
688 microdigestion methods. Geochimica et Cosmochimica Acta, 68, 1591-1606.
689 Pouchou J.L. and Pichoir F. (1985): "PAP" φ(rZ) procedure for improved quantitative
690 microanalysis. *Microbeam Analytics* 1985, 104-106.
691 Ritherdon, B., Phelps, C., Neff, H., Sowder, A.G., and Clark, S.B. (2003) Stability of U(VI) solid
692 phases in the U(VI)-Ca2+-SiO2-OH system. Radiochimica Acta, 91, 93–96.
693 Reich, T. Moll, H., Arnold, T., Denecke, M.A., Hennig, C., Geipel, G., Bernhard, G., Nitsche, H.,
694 Allen, P.G., Bucher, J.J., Edelstein, N.M. and Shuh, D.K. (1998) An EXAFS study of
695 uranium(VI) sorption onto silica gel and ferrihydrite. Journal of Electron Spectroscopy
696 Related Phenomena, 96, 237-243.
697 Schindler, M., Durocher, J, Abdu, Y. and Hawthorne, F.C. (2009a): Hydrous silica coatings:
698 Occurrence, Speciation of Metals and Environmental Significance. Environmental
699 Science and Technology, 43, 8775–8780.
700 Schindler, M., Freund, M., Hawthorne, F.C., and Burns, P.C. (2009b) XPS spectra of uranyl
701 minerals and synthetics. I. The U 4f Spectrum. Geochimica et Cosmochimica Acta, 73,
702 2471-2487.
703 Schindler, M., Freund, M., Hawthorne, F.C., and Burns, P.C. (2009c): XPS spectra of uranyl
704 minerals and synthetics. II. The O 1s Spectrum. Geochimica et Cosmochimica Acta, 73,
705 2488-2509.
706 Schindler, M., Fayek, M., and Hawthorne, F.C. (2010) Uranium-rich opal from the Nopal I
707 uranium deposit, Peña Blanca, Mexico: evidence for the uptake and retardation of
708 radionuclides. Geochimica et Cosmochimica Acta, 74, 187–202.
709 Schindler, M., Legrand, C.A., and Hochella, M.F. (2015) Alteration, adsorption and nucleation
710 processes on clay-water interfaces: Mechanisms for the retention of uranium by altered
711 clay surface on the nanometer scale. Geochimica et Cosmochimica Acta, 153, 15-36.

712 Schindler, M. and Hochella, M.F. (2015) Soil memory in mineral surface coatings: environmental
713 processes recorded at the nanoscale. Geology 43, 415–418.
714 Shao, H.B., Kosakowski, G., Berner, U., Kulik, D.A., Mader, U. and Kolditz, O. (2013) Reactive
715 transport modeling of the clogging process at Maqarin analogue site. Physics and
716 Chemistry of the Earth 64, 21-31.
717 Shawe, D.R. (1972) Reconnaissance geology and mineral potential of the Thomas, Keg, and
718 Desert calderas, central Juab County, Utah: U.S. Geological Survey Professional Paper
719 800–B, pp. B67–B77.
720 Schwyn, B., Wersin, P., Rüedi, J., Schneider, J., Altmann, S., Missana,T. and Noseck, U.
721 (2012) FUNMIG Integrated Project results and conclusions from a safety case
722 perspective. Applied Geochemistry, 27, 501–515.
723 Shirley D.A. (1972) High-resolution X-ray photoemission spectrum of the valence bands of gold.
724 Physical Review, B5, 4709-4714.
725 Smellie, J.A.T. and Karlsson, F. (1999) The use of natural analogues to assess radionuclide
726 transport. *Engineering Geology* **52**, 193-220.
727 Smith, K.F., Bryan, N.D. Swinburne, A.D., Bots, P. Shaw, S., Natrajan, L.S., Frederick, J.,
728 Mosselmans, W., Livens, F.R., and Morris, K. (2015) U(VI) behaviour in hyperalkaline
729 calcite systems. Geochimica et Cosmochimica Acta 148, 343–359.
730 Soderholm, L., Skanthakumar, S., Gorman-Lewis, D., Jensen, M. P., and Nagy, K. L.(2008)
731 Characterizing solution and solid-phase amorphous uranyl silicates. Geochimica et
732 Cosmochimica Acta, *72*, 140–150.
733 Stein, C. L. and Kirkpatrick, R. J. 1976. Experimental porcelanite recrystallization kinetics; a
734 nucleation and growth model. Journal of Sedimentary Research. 46, 2, 430 - 435.
735 Sylwester, E. R., Hudson, E. A., and Allen, P. G. (2000) The structure of uranium (VI) sorption
736 complexes on silica, alumina, and montmorillonite. *Geochimica et Cosmochimica Acta*
737 64, 2431–2438.

738 Szabo, B.J. and Kyser, T.K. (1990) Ages and stable isotope compositions of secondary calcite
739 and opal in drill cores from Tertiary volcanic rocks of the Yucca Mountain area, Nevada.
740 Geological Society American Bulletin, 102, 1714-1719.
741 Techer, I., Khoury, H.N., Salameh, E., Rassineux, F., Claude, C., Clauer, N., Pagel, M.,
742 Lancelot, J., Hamelin, B., and Jacquot, E. (2006) Propagation of high-alkaline fluids in
743 an argillaceous formation: Case study of the Khushaym Matruk natural analogue
744 (Central Jordan). Journal of Geochemical Exploration 90, 53–67.
745 Tran, H.H., Roddick , F.A., and O'Donnell, J.A. (1999) Comparison of chromatography and
746 desiccant silica gels for the adsorption of metal ions—I. adsorption and kinetics. Water
747 Research 33, 2992–3000.
748 VanDamme H. (2000) Nanoscale and mesoscale morphology of silica surfaces. In Absorption
749 on silica surfaces: Surfactant Science Series. Ed. Papirer U. Marcel Dekker, Ney York,
750 p.119-166.
751 Wagner C.D, Riggs W.M., Davis L.E., Moulder J.F. and Mailenberg G.M (1979) Handbook of X-
752 ray photoelectron spectroscopy. Perkin-Elmer.
753 Whelan J.F., Paces J.B. and Peterman Z.E. (2002) Physical and stable-isotope evidence form
754 formation of secondary calcite and silica in the unsaturated zone, Yucca Mountain,
755 Nevada. Applied Geochemistry, 17, 735-750.
756 Williams, L. A. and Crerar, D. A. (1985) Silica diagenesis, II. General mechanisms. Journal of
757 Sedimentary Petrology. 55, 312 - 321.
758 Williams, L. A., Parks, G. A. and Crerar, D. A. (1985) Silica diagenesis, I. Solubility controls.
759 Journal of Sedimentary Petrology. 55, 301 - 311.
760 Wood, S.A. (1992) Theoretical prediction of speciation and solubility of beryllium in
761 hydrothermal solution to 300°C at saturated vapor pressure: Application to
762 bertrandite/phenakite deposits: Ore Geology Reviews, 7, 249–278.

763 Zheng Y.-F. (1991). Calculation of oxygen isotope fractionation in metal oxides. Geochemica et
764 Cosmochimica Acta, 55, 2299-2307.
765 Zielinski, R.A., Ludwig, K.R., and Lindsey, D.A. (1977) Uranium lead apparent ages of
766 uraniferous secondary silica as a guide for describing uranium mobility, in: Short Papers
767 of the U.S. Geological Survey Uranium-Thorium Symposium, J.A. Campbell, ed., U.S.
768 Geological Survey Circular, 753, 39.
769 Zielinski, R.A. (1980) Uranium in secondary silica: a possible exploration guide. Economic
770 Geology, 75, 592–602.
771
772
773
774
775
776
777
778
779
780
781
782
783
784
785
786
787

This is a preprint, the final version is subject to change, of the American Mineralogist (MSA)
Cite as Authors (Year) Title. American Mineralogist, in press.
(DOI will not work until issue is live.) DOI: http://dx.doi.org/10.2138/am-2017-5700

788 **Table 1. Uraniferous opal samples, their location, paragenesis, appearance, U0-Pb age**

789 **and the analytical method used for each sample.**

Sample	Location	appearance	paragenesis	U-Pb age[1]	Analytical methods
DL-U18B	Autunite No. 8 Prospect, Thomas Range	Distinct zones of fibrous opal CT (lussatite) quartz, morganite violet in U rich zones	quartz, moganite K-feldspar vorlanite	3.81 m.y.	EMPA SIMS XRD Raman
DL-N22	Roadside Be Mine, Beryllium tuff member of Spor Mountain	Massy opal CT, mottled texture, Distinct zoning; violet in U-rich zones	fluorite bertrandite vorlanite Mn-oxide	14 ± 3 m.y	LA-ICP-MS SIMS Raman XRD
M3N	Monitor Be Prospect, Beryllium tuff member of Spor Mountain	Yellow massy opal CT, mottled texture, nodule	fluorite vorlanite	8.06-8.9 m.y	EMPA SIMS XPS Raman SEM
Rd	Altered tuff associated with the beryllium ore.	Violet	K-feldspar montmorrilonite pyrolisite cryptomelane fluorite opal-CT	21 m.y.	SEM XRD SIMS

790 1. From Ludwig et al. (1980)

791

Table 2. Uranium concentration and O-isotope composition of the opals and pyrolusite

Opal sample and zones	U min. and max. [mgkg^{-1}]	U average [mgkg^{-1}]	δ^{18}O-value [‰] min. and max.	δ^{18}O-value [‰] Average
DL-U18B (EMPA)	50-3093	1038	n.a.	n.a.
Lissotite *A2-A4* (SIMS)	960-2000	1370	19.6-20.5	20.0
Quartz, *A1, A5-A6* (SIMS)	66-668	320	18.4-20.8	19.5
Moganite (M) + transition zone (TR); *B1-B2*, (SIMS)	54 (M) 58-574 (TR)	54 (M) 220	9.6 (M) 11.9-14.1 (TR)	9.6 (M) 13.0(TR)
M3N Massy opal	EMPA: 75-6342 SIMS: 1617-2739	3011 2148	12.7-19.9	16.5
DL-N22 Massy opal	LA-ICP-MS: 480-1572 SIMS: 278-1545	 907 710	15.8-22.3	18.9
Altered pyrolusite crystals	n.a	n.a	-7.9 - -9.5	-8.6
Finely disseminated pyrolusite	n.a	n.a	-7.1 - -10.2	-8.9

792

793

794

795

796

797

798 **Figure Captions**

799 FIGURE 1. a) Optical image of an altered rhyolite (sample Rd); the area mainly composed of
800 fluorite is labelled *Fl*; (b) SEM in BSE mode of altered crystals (cr) and disseminated (di)
801 pyrolusite in a fluorite matrix; (c) Optical image of the opal sample *DL-U18B*. Infillings of fluorite-
802 bearing opals are white to violet; (d)-(e) chemical distribution maps of (d) Ca and (e) U in the
803 sample; (f) the concentration of U versus Ca on the basis of 24 spot analyses with an electron
804 microprobe.

805

806 FIGURE 2. (a) Selected positions of the SIMS spot analyses along the traverse from *A1* to *B2;*
807 (b) chemical distribution map for U indicating the location of selected spot analyses (labelled *A2,*
808 *A3, A4, A5-A6, B1-B2*; (c) measured $\delta^{18}O$ values along the traverse, values corresponding to
809 the spots *A1, A6, B1* and *B2* are labelled;. (d) Raman spectra taken at eight different locations,
810 which occur in proximity to selected SIMS spot analyses; characteristic peaks for opal-CT,
811 quartz and moganite are labelled *Op*, *Q* and *M*, respectively.

812

813 FIGURE 3. (a) Raman spectrum of area A4 which is predominantly composed of opal-CT; (b)-
814 (c) Raman spectra of (b) cristobalite (*Cr*) and (c) tridymite (*Tr*), modified from Ilieva et al. 2007;
815 (d) XRD powder diffraction pattern of the opal-CT samples *M3N*, *DL-U18B* and *DL-N22*; the
816 patterns are labelled accordingly; vertical bars indicate peaks and shoulders corresponding to
817 the structural components cristobalite (*Cr*) and tridymite (*Tr*); d-spacings of the different
818 components and FWHM of the bands are indicated

819

820

821

822

FIGURE 4. High resolution optical images of the opal modifications *DL-U18B*, *M3N* and *DL-N22;* the images are labelled accordingly; bands of fibrous opal-CT, microcrystalline quartz and moganite are labelled in the optical image for DL-U18B as *Op*, *Q* and *M*, respectively. (b) high resolution optical image of the interface between the zones *A1* and *A2* of the examined traverse in sample DL-U18B; the high abundance of red crystal along the interface is clearly visible.

FIGURE 5. (a) Optical image of the yellowish-brown outer shell of the opal sample *M3N*, a traverse of spot analyses is labelled with a black line and the letters *A* and *B*; (b)-(c) chemical-distribution maps of (b) Ca and (c) U; (d) optical image indicating a traverse of spot analyses from *A* to *B*; (e) concentration of U versus Ca on the basis of 24 spot analyses with an electron microprobe; (f)-(g) Position of the spot analyses along the traverse from *A* to *B* versus the respective (f) concentration of U and (g) $\delta^{18}O$ value.

FIGURE 6. U $4f_{7/2}$ spectra of opal sample *M3N* and a yellow and greenish opalline rock- coating sample from Nopal 1, Pena Blanca, Mexico; the location of the bands for the U^{6+} and U^{5+}/U^{4+} components are indicated with vertical bars.

FIGURE 7. (a) Optical image of opal sample *DL-N22*; a traverse from *A* to *C* measured as a line scan with LA-ICP-MS is indicated; a traverse of spot analyses were measured with SIMS from *A* to *B*; three different zones can be recognized from the colour of the opal (labelled *A*, *B* and *C*), the corresponding elemental relation between U and Ca in the silica-rich zones and the mineralogical composition in the silica-depleted zone are indicated; (b) LA-ICP-MS line scans for U, Ca and Si along the traverse from A to *B* and to *C*; an U-enriched boundary between zone *B* and *C* is encircled; (c)-(e) Position of the spot analyses along the traverse from *A* to *B* versus the respective (c) concentration of U, (d) $\delta^{18}O$ value and (e) F /O CPS ratio.

FIGURE 8. (a)-(b) plot of the concentrations of (a) Ca versus U and (b) Mn versus U on the basis of the quantification of different sections in LA-ICP-MS line scans; (c) chemical-distribution maps of F, Ca and Mn in the fluorite-pyrolusite enriched zone of *DL-U18B*; the maps are labelled with the corresponding element.

This is a preprint, the final version is subject to change, of the American Mineralogist (MSA)
Cite as Authors (Year) Title. American Mineralogist, in press.
(DOI will not work until issue is live.) DOI: http://dx.doi.org/10.2138/am-2017-5700

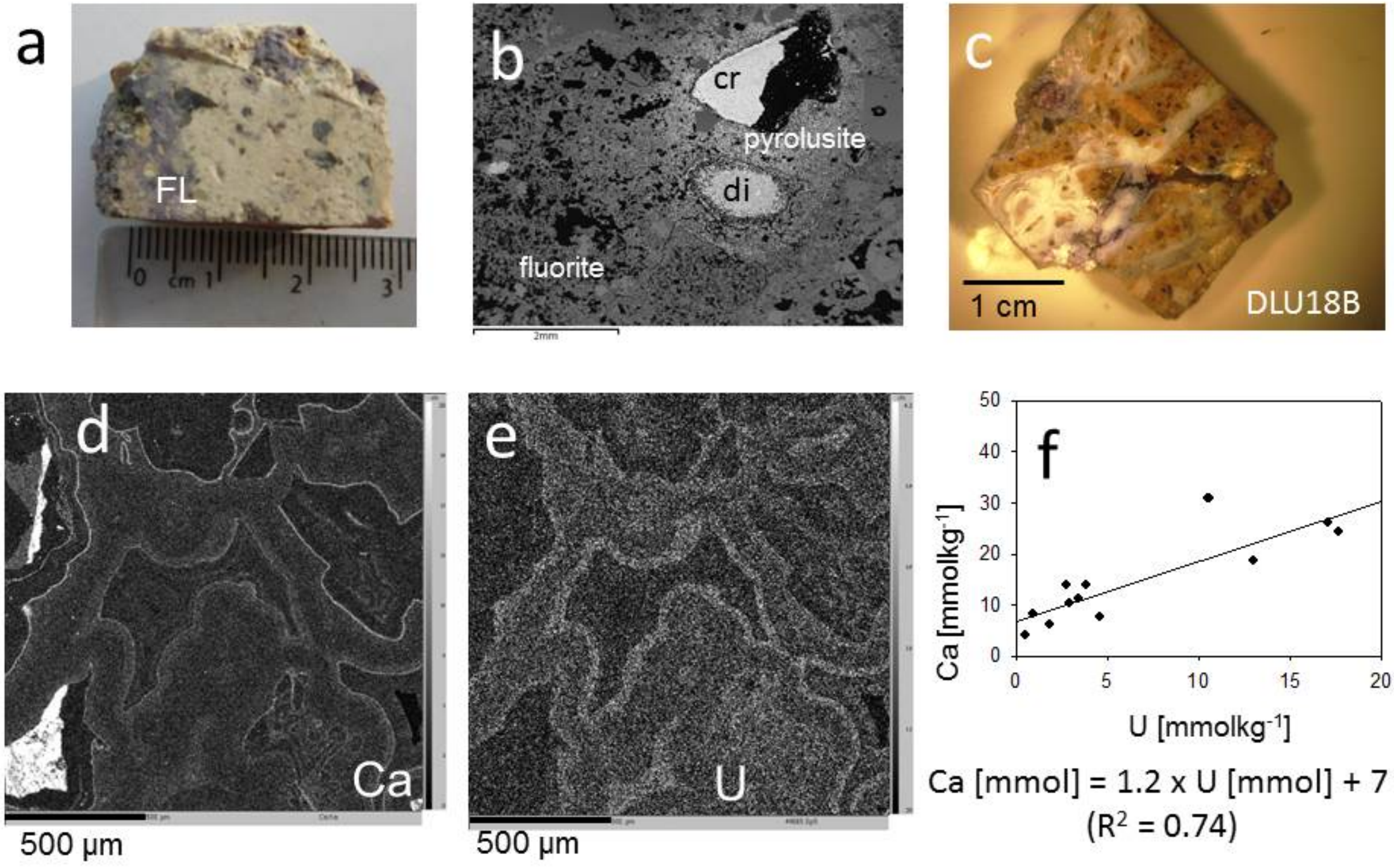

Figure 1

This is a preprint, the final version is subject to change, of the American Mineralogist (MSA)
Cite as Authors (Year) Title. American Mineralogist, in press.
(DOI will not work until issue is live.) DOI: http://dx.doi.org/10.2138/am-2017-5700

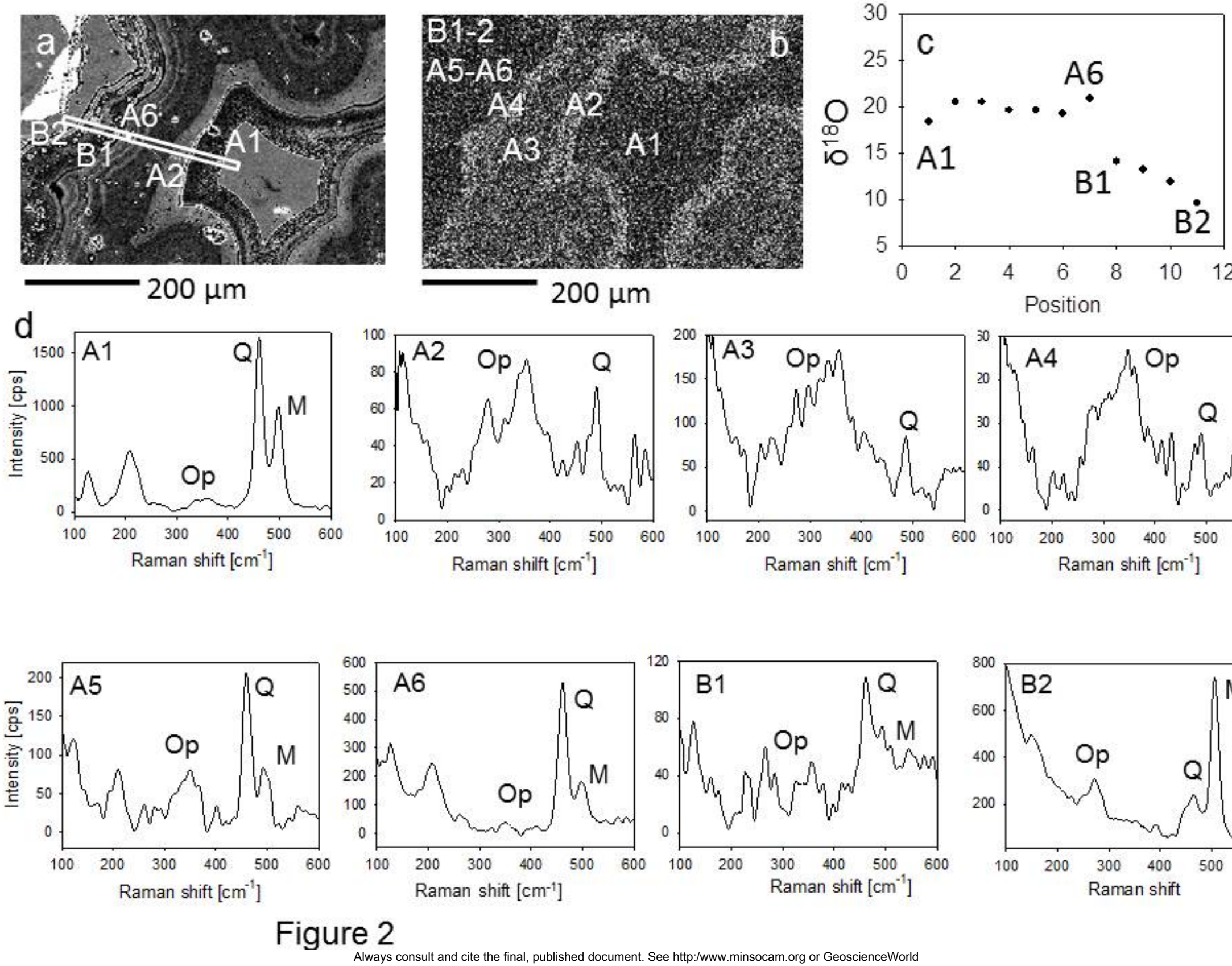

Figure 2

This is a preprint, the final version is subject to change, of the American Mineralogist (MSA)
Cite as Authors (Year) Title. American Mineralogist, in press.
(DOI will not work until issue is live.) DOI: http://dx.doi.org/10.2138/am-2017-5700

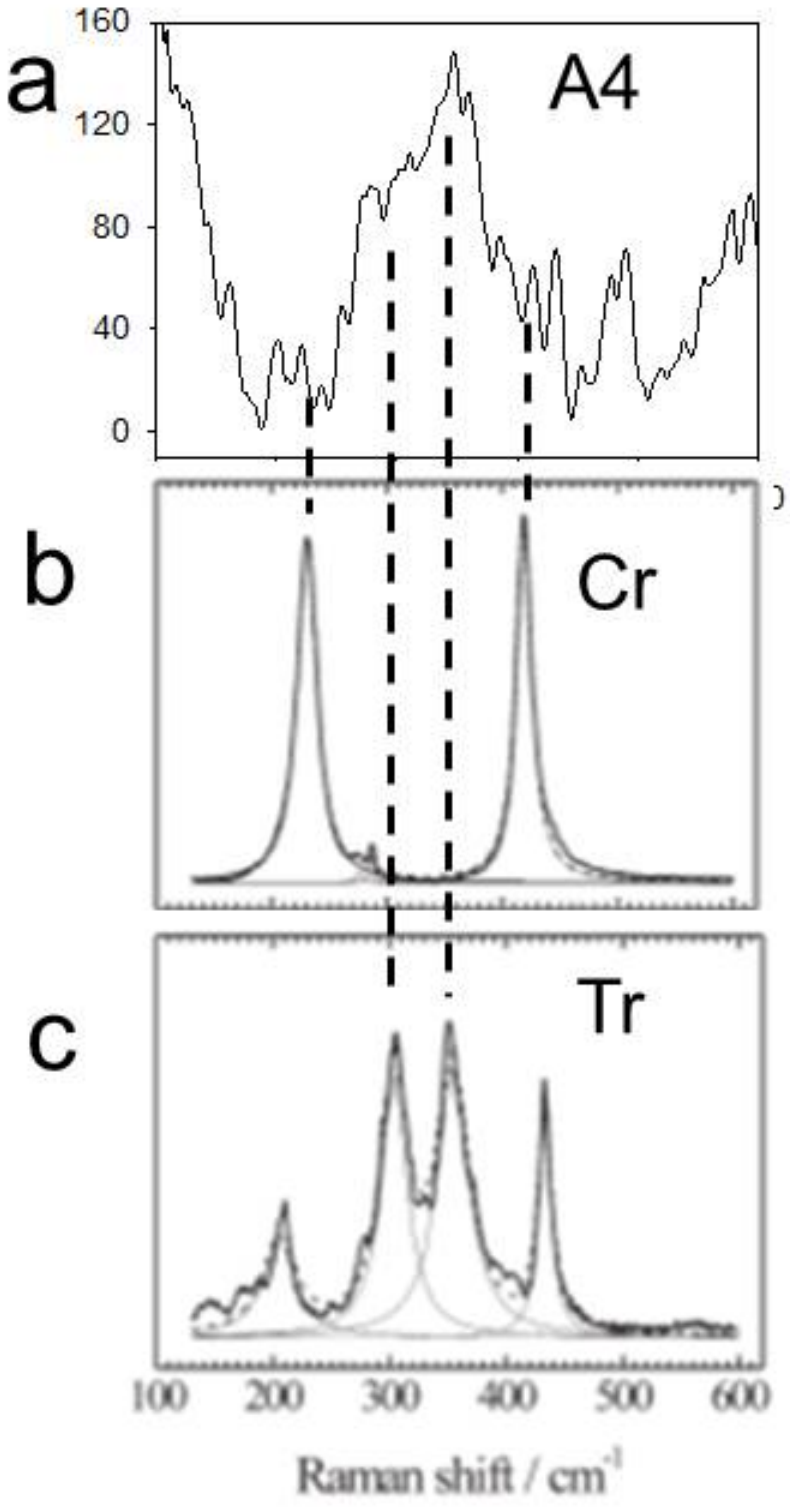

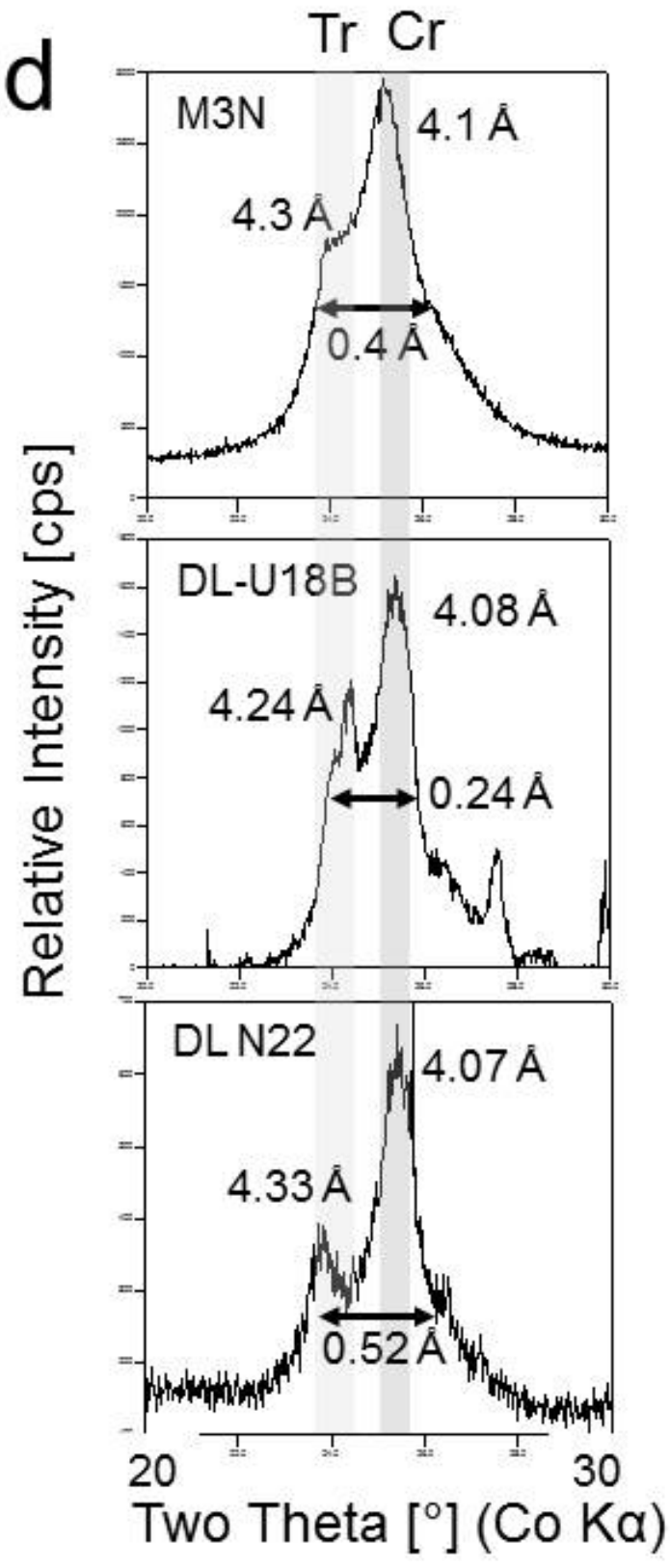

Figure 3

This is a preprint, the final version is subject to change, of the American Mineralogist (MSA)
Cite as Authors (Year) Title. American Mineralogist, in press.
(DOI will not work until issue is live.) DOI: http://dx.doi.org/10.2138/am-2017-5700

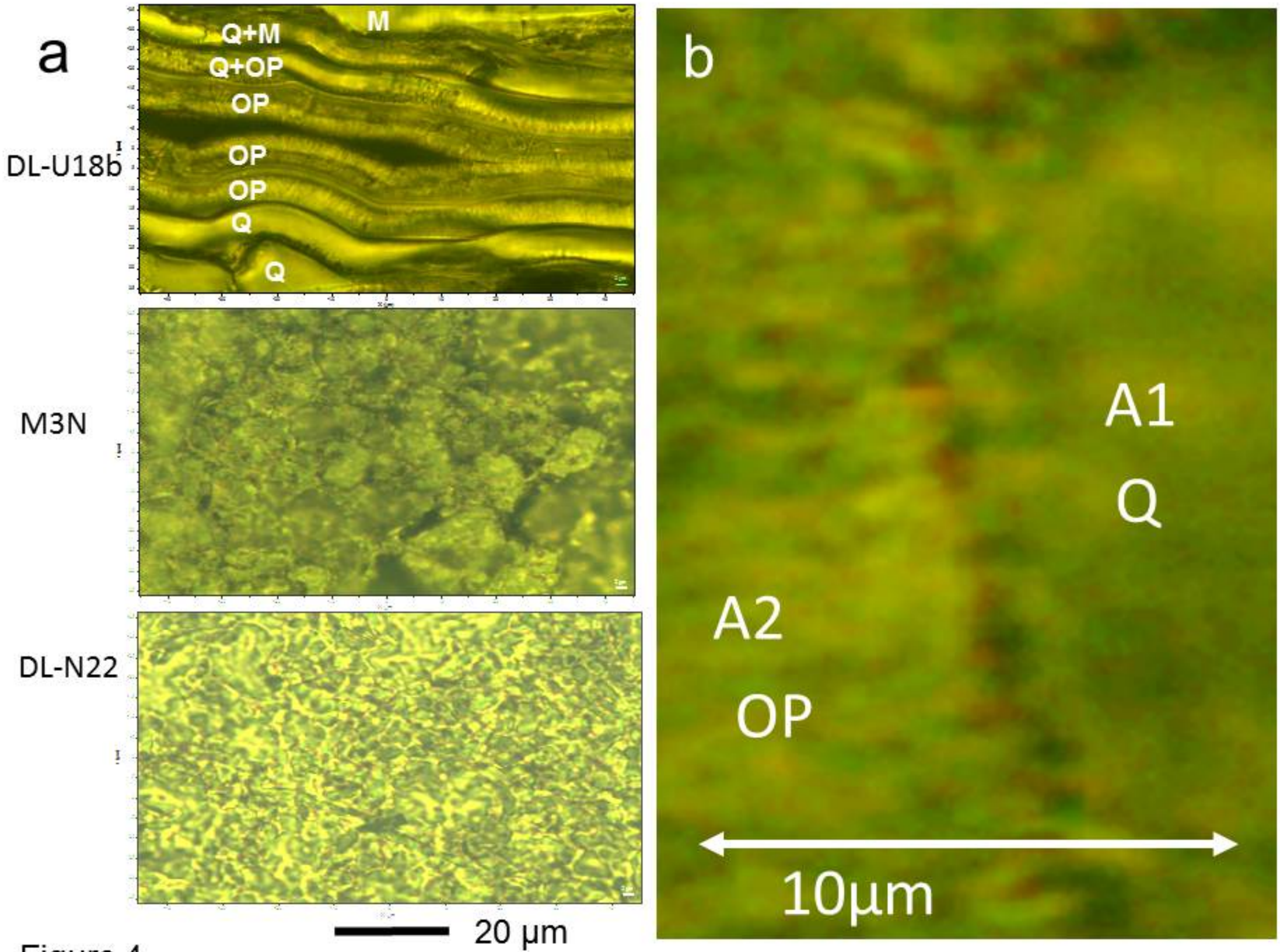

Figure 4

This is a preprint, the final version is subject to change, of the American Mineralogist (MSA)
Cite as Authors (Year) Title. American Mineralogist, in press.
(DOI will not work until issue is live.) DOI: http://dx.doi.org/10.2138/am-2017-5700

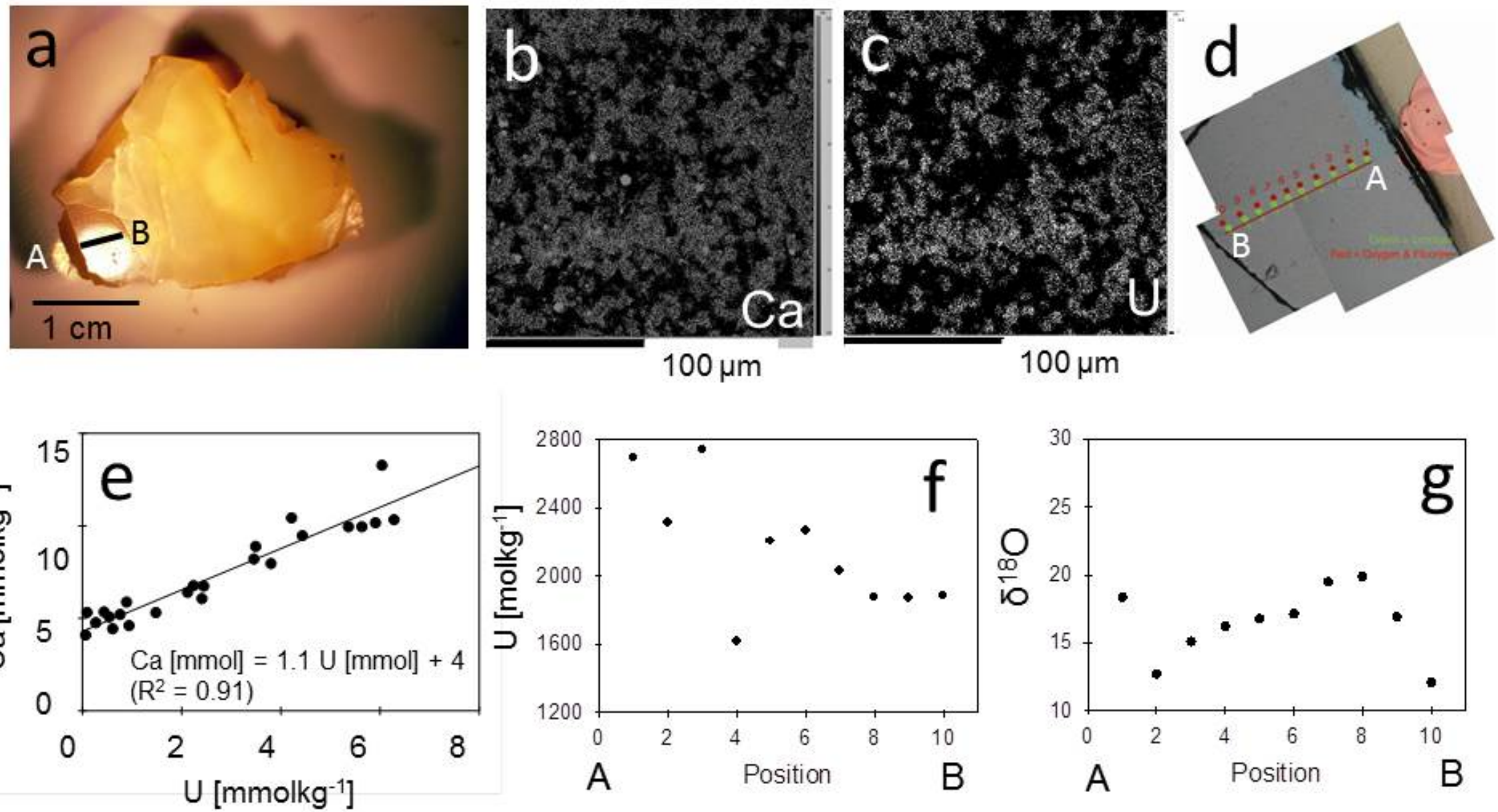

Figure 5

This is a preprint, the final version is subject to change, of the American Mineralogist (MSA)
Cite as Authors (Year) Title. American Mineralogist, in press.
(DOI will not work until issue is live.) DOI: http://dx.doi.org/10.2138/am-2017-5700

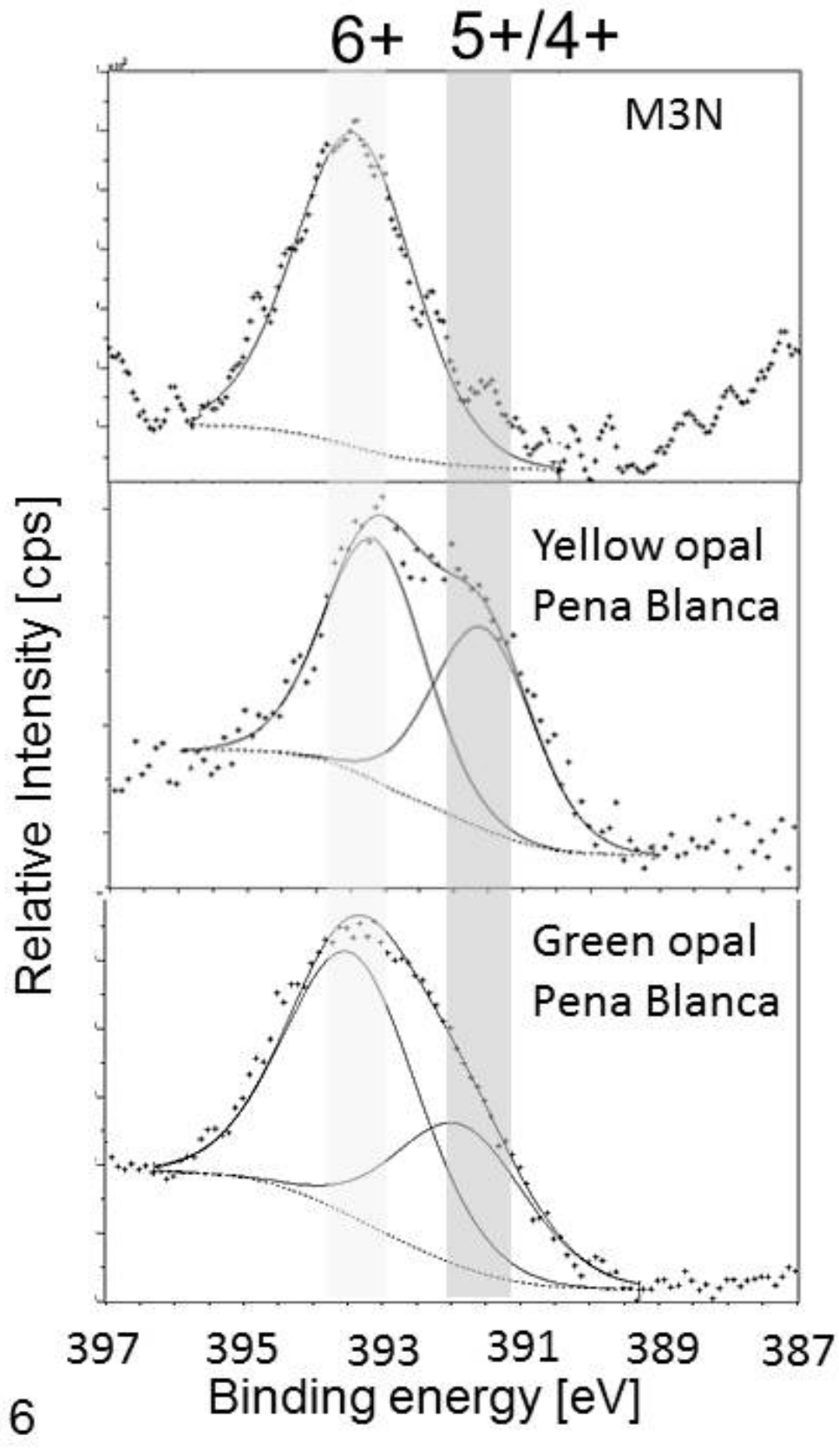

Figure 6

This is a preprint, the final version is subject to change, of the American Mineralogist (MSA)
Cite as Authors (Year) Title. American Mineralogist, in press.
(DOI will not work until issue is live.) DOI: http://dx.doi.org/10.2138/am-2017-5700

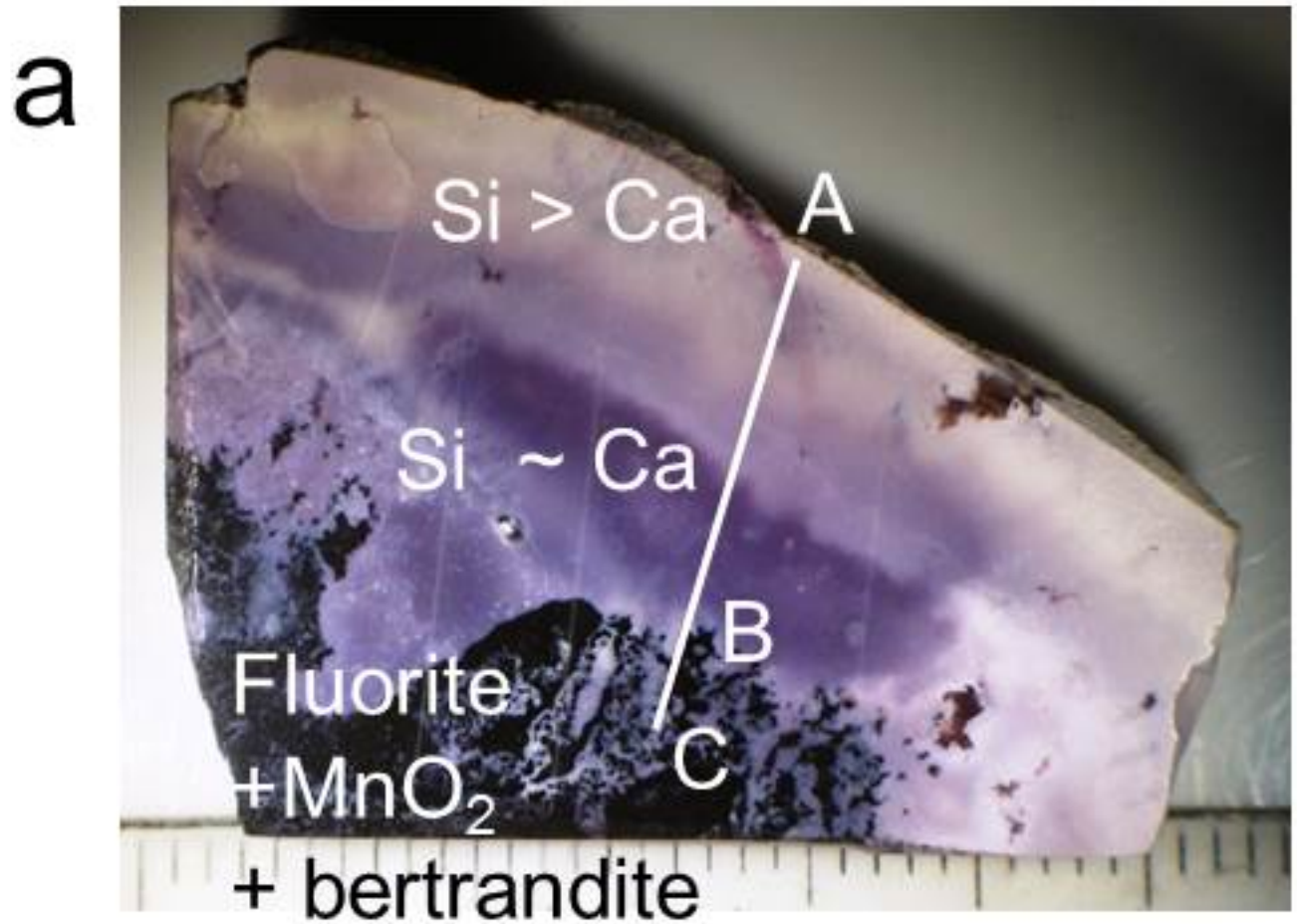

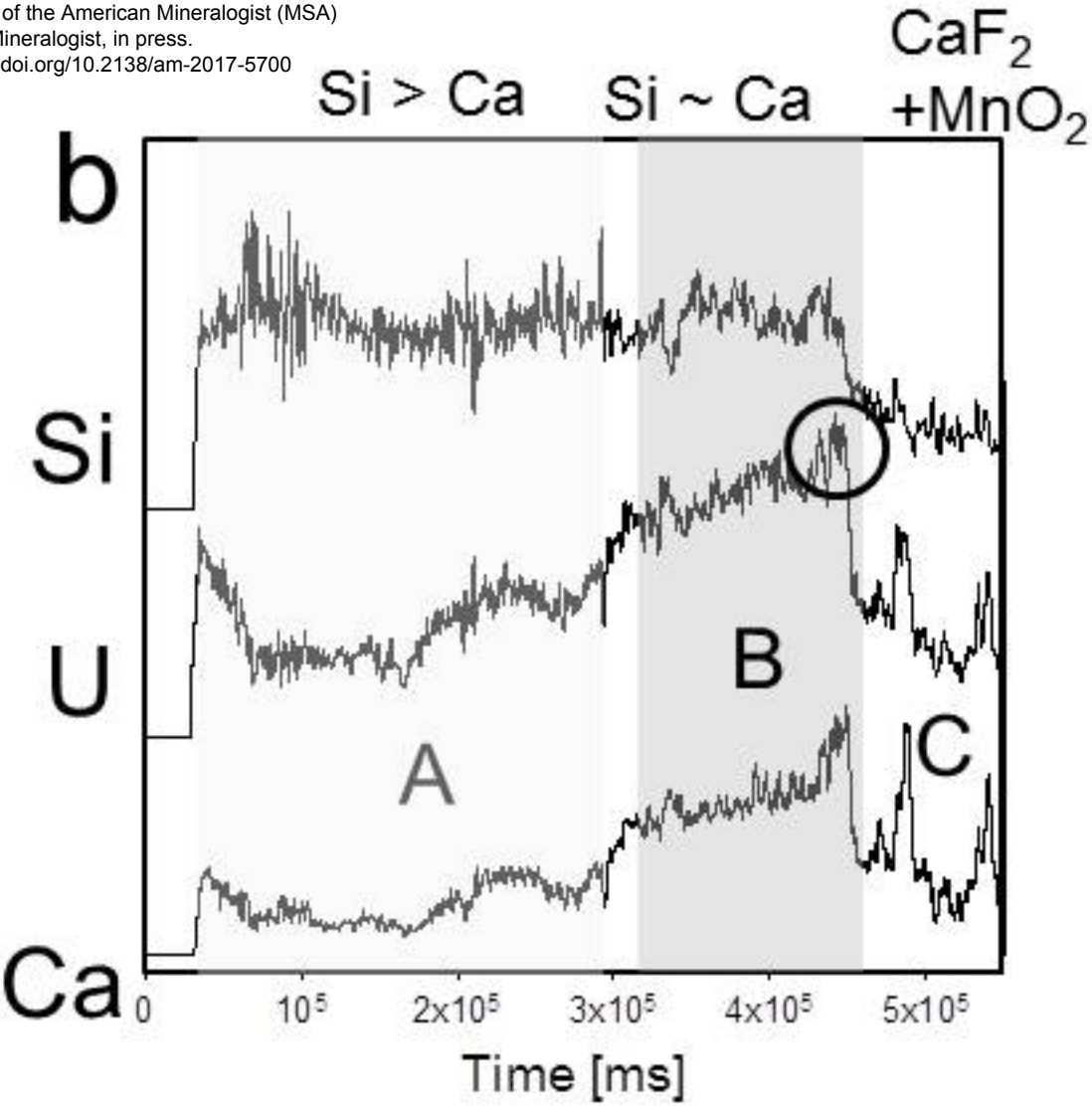

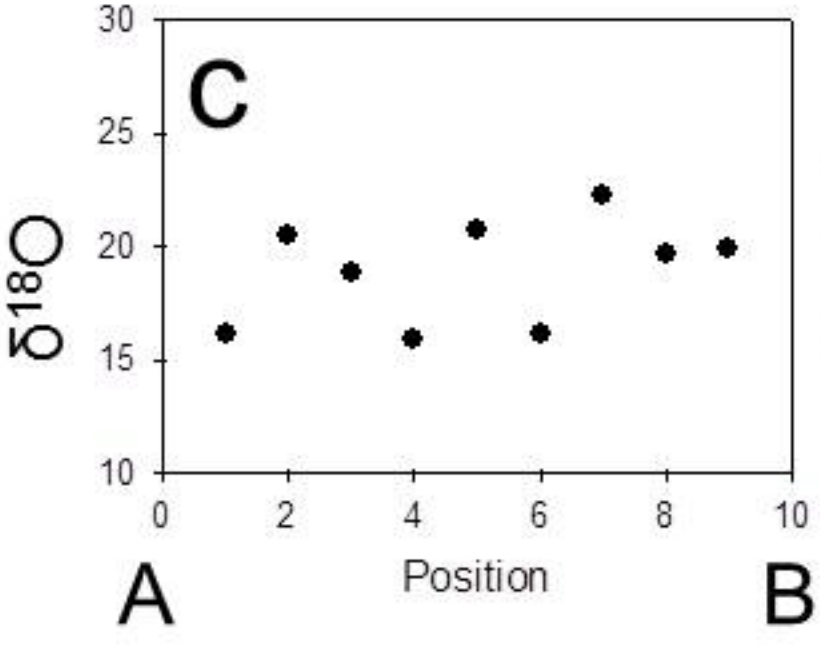

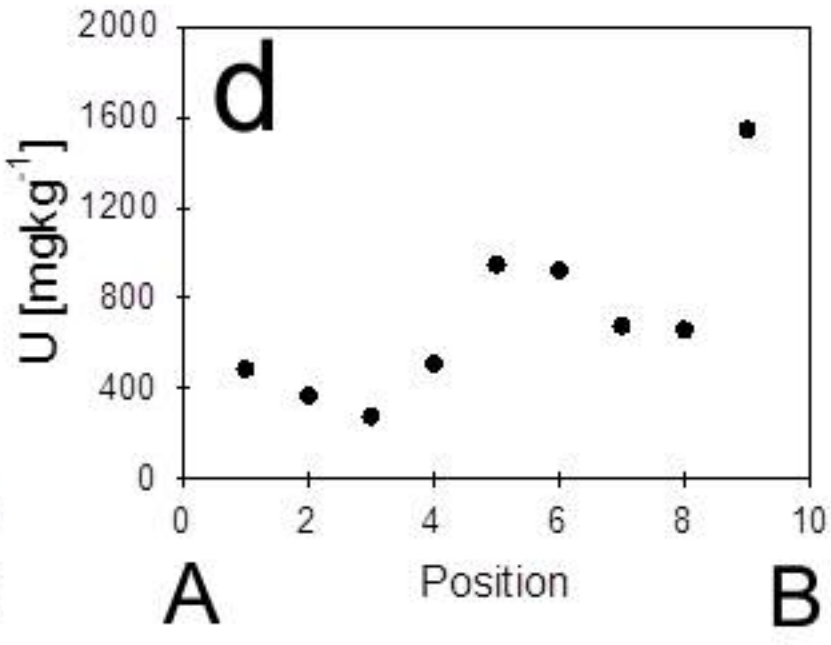

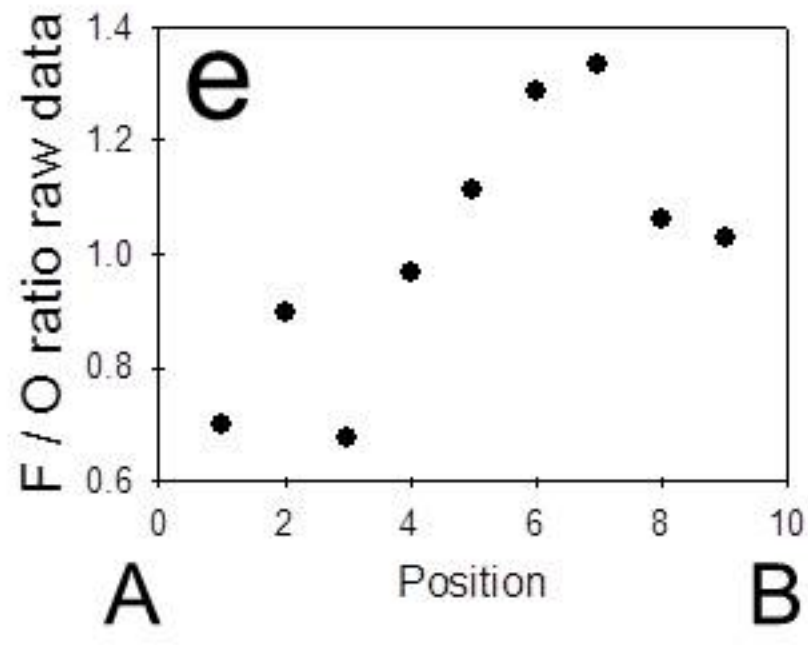

Figure 7

This is a preprint, the final version is subject to change, of the American Mineralogist (MSA)
Cite as Authors (Year) Title. American Mineralogist, in press.
(DOI will not work until issue is live.) DOI: http://dx.doi.org/10.2138/am-2017-5700

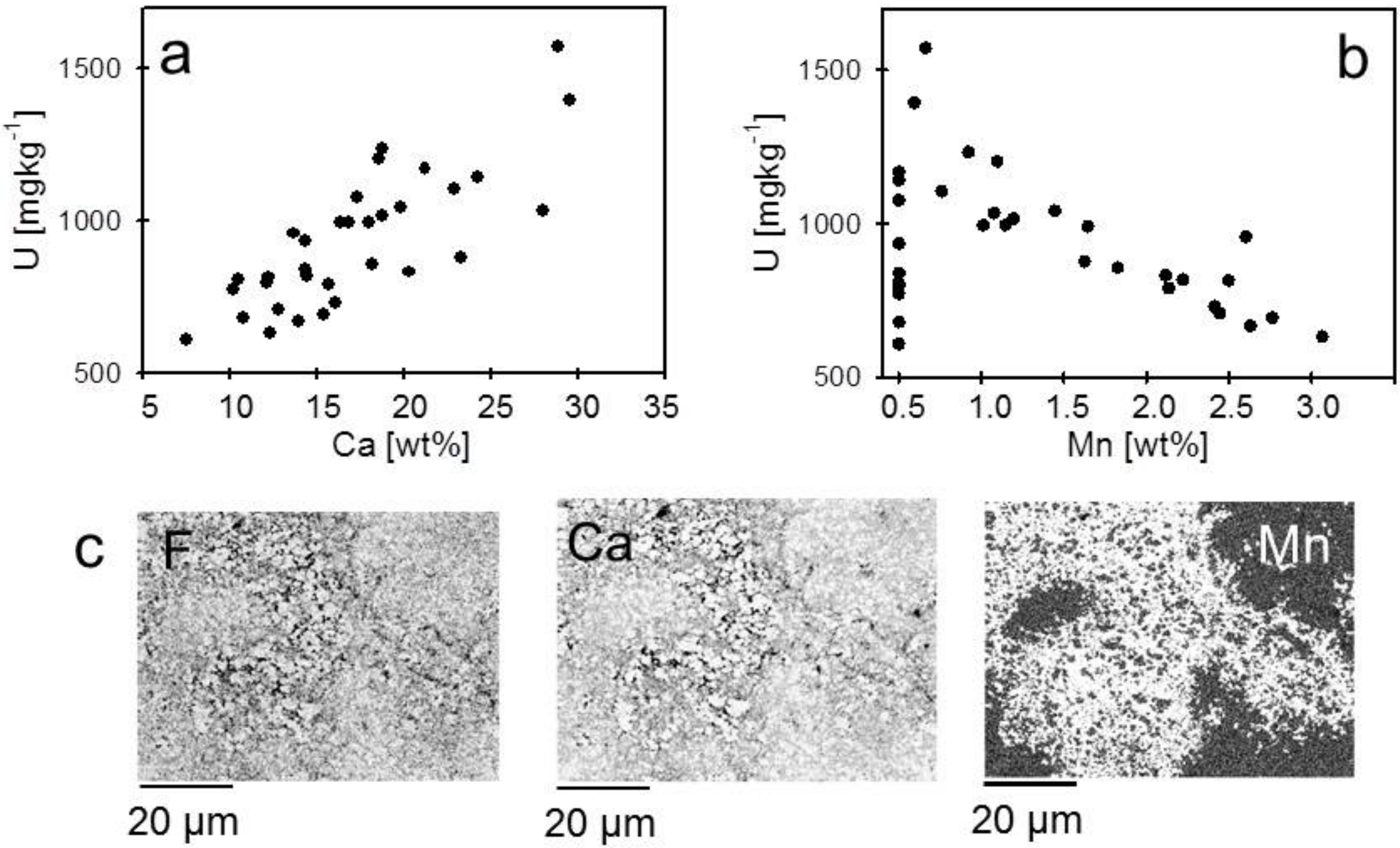

Figure 8